Magnetically recyclable TiO$_2$/MXene/MnFe$_2$O$_4$ photocatalyst for enhanced peroxymonosulphate-assisted photocatalytic degradation of carbamazepine and ibuprofen under simulated solar light

Anna Grzegórska [a],*, Joseph Chibueze Ofoegbu [b], Laura Cervera-Gabalda [c], Cristina Gómez-Polo [c], Diana Sannino [b], Anna Zielińska-Jurek [a],*

[a] Department of Process Engineering and Chemical Technology, Faculty of Chemistry, Gdańsk University of Technology, G. Narutowicza 11/12, 80-233 Gdańsk, Poland
[b] Department of Industrial Engineering, University of Salerno, via Giovanni Paolo II, 132, 84084 Fisciano, Italy
[c] Departamento de Ciencias-INAMAT2, Universidad Pública de Navarra, Campus de Arrosadia, 31006 Pamplona, Spain

ARTICLE INFO

ABSTRACT

In this study, a novel TiO$_2$/Ti$_3$C$_2$/MnFe$_2$O$_4$ magnetic photocatalyst with dual properties, enabling (i) improved photocatalytic degradation with PMS activation under simulated solar light and (ii) magnetic separation after the degradation process in an external magnetic field was developed and applied for the efficient photodegradation pharmaceutically active compounds (PhACs) frequently present in wastewater and surface waters worldwide. MXene was used as a Ti precursor for anatase/rutile synthesis and as a co-catalyst in the photodegradation process. Manganese ferrite with ferrimagnetic properties was coupled with the TiO$_2$/Ti$_3$C$_2$ composite to facilitate the magnetic separation after the purification process in an external magnetic field. Moreover, MnFe$_2$O$_4$ was used for PMS activation, producing •SO$_4^-$ radicals with a strong oxidation ability and higher redox potential of 2.5–3.1 V (vs. NHE) than •OH radicals with a standard oxidation–reduction potential of 2.8 V. The effect of the manganese ferrite content in the composite structure (5 wt% and 20 wt%) on the physicochemical properties and photocatalytic activity of the magnetic photocatalyst was investigated. Furthermore, the most photocatalytic active composite of TiO$_2$/MXene/5%MnFe$_2$O$_4$ was used for peroxymonosulphate-assisted photocatalytic degradation of ibuprofen and carbamazepine. The effect of peroxymonosulphate concentration (0.0625 mM, 0.125 mM, and 0.25 mM) and the synergistic effect of PMS activation on photocatalytic degradation was studied. Based on the obtained results, it was found that TiO$_2$/MXene/5%MnFe$_2$O$_4$/PMS process is an efficient advanced treatment technology for the oxidation of emerging contaminants that are not susceptible to biodegradation. Carbamazepine and ibuprofen were completely degraded within 20 min and 10 min of the PMS-assisted photodegradation process under simulated solar light. The trapping experiments confirmed that •SO$_4^-$ and •O$_2^-$ are the main oxidising species involved in the CBZ degradation, while •SO$_4^-$ and h$^+$ in the IBP degradation. Furthermore, introducing interfering ions of Na$^+$, Ca^{2+}, Mg^{2+}, Cl$^-$, and SO$_4^{2-}$ in the model seawater did not affect the removal efficiency of both pharmaceuticals. In terms of reusability, the performance of the TiO$_2$/MXene/5%MnFe$_2$O$_4$/PMS photocatalyst was stable after four subsequent cycles of carbamazepine and ibuprofen degradation.

1. Introduction

Emerging contaminants in aquatic systems arising from drug residues have received great attention recently. All these compounds may be excreted into the environment as a mixture of the parent compound and its metabolites because they are only partially degraded and removed in biological wastewater treatment plants [1,2] Moreover,

some of them undergo various attenuation processes, including biotransformation, photolysis, sorption, and volatilisation [3].

Among them, ibuprofen (IBP) and carbamazepine (CBZ) are the most frequently detected drugs in aquatic ecosystems [4]. Ibuprofen (IBP) is a non-steroidal anti-inflammatory drug with nearly 200 tons worldwide annual consumption. Carbamazepine (CBZ) is an anticonvulsant and antiepileptic pharmaceutical, with worldwide consumption above 1000

---

tons per year, which is also used in the treatment of trigeminal neuralgia, a chronic pain disorder [5].

The concentrations of both pharmaceuticals in wastewater treatment plant effluents range from hundreds ng/dm^3 to tens of μg/dm^3. The effluents from Portugal WWTPs contained 1059 ng/dm^3 of CBZ and 217 ng/dm^3 of IBP [6]. Meanwhile, IBP has been detected in the Tunisia WWTPs effluent from 8 to 43 μg/dm^3. The concentration of CBZ was determined at a level between 60 and 132 μg/dm^3 [7]. Carbamazepine has also been detected in coastal and offshore seawaters of the Baltic Sea, where the concentrations were low. However, due to the long turnover time and low removal efficiency, a stock of over 55 t of carbamazepine has accumulated in the Baltic Sea waters [8]. Carbamazepine and ibuprofen can generate subtle effects on aquatic and terrestrial organisms. For example, carbamazepine and ibuprofen can modify physiological and biochemical processes in Senegalese sole (Solea senegalensis) and interfere with the biosynthesis of enzymes involved in the osmoregulatory process [9]. Therefore, improving water treatment technology is the active subject matter of actual research to protect ecosystems, increase water quality and ensure the sustainability of water cycle management.

The advanced oxidation processes (AOP), based on the in-situ generation of the strongest oxidants - hydroxyl radicals and sulphate radicals, have been recognised as a promising approach for wastewater treatment from residues of recalcitrant and emerging organic contaminants [10,11]. Among the AOPs, ozonation and UV irradiation have already been established and started at full scale for the treatment of drinking water and the facilities of water reuse. Recently, the photo-Fenton process, UV/O$_3$, and UV/H$_2$O$_2$ have been commonly applied to remove persistent organic compounds such as carbamazepine and ibuprofen to strengthen the oxidation capability [12–15]. Nevertheless, ozonation is restricted by the high cost of ozone and low mineralisation efficiency, while the Fenton process usually operates under a limited pH range (3–4) and generates Fe(OH)$_3$ precipitation [16–18]. The photocatalysis process is a promising intensification approach in AOPs, owing to the generation of electron-hole pairs under light irradiation and the production of reactive oxygen species. At present, solar-induced chemical processes, such as photocatalysis, are limited by low quantum efficiencies [19].

In this regard, the twofold strategy to optimise photocatalyst structure towards the degradation of selected PhACs was investigated in this study. Previously, it was reported that the hybridisation of semiconductor with graphene-related materials improve charge carriers mobility [20]. Recently, MXenes, the family of early transition metal carbides, have been proposed as advanced carbon-based materials, which may act as co-catalysts, enhancing the adsorption of the pollutants on the surface, photocatalyst stability, and increasing the light absorption range. Significantly in situ oxidation of MXene Ti$_3$C$_2$T$_x$ led to the formation of TiO$_2$/Ti$_3$C$_2$ composite with intimate contact providing effective charge carriers separation. Therefore, Ti$_3$C$_2$/TiO$_2$ composites have been proposed as advanced candidates with high efficiency in photocatalytic process [21,22]. This hybrid material with strong bonding possesses minimised defects at the interfaces [23,24]. Based on the studies performed in our group, we showed markedly enhanced photocatalytic activity of accordion-like TiO$_2$/Ti$_3$C$_2$ composites with exposed {1 0 1} and {0 0 1} TiO$_2$ crystal facets [21,22].

Furthermore, considering the difficulties of separation and recycling of photocatalyst nanoparticles from wastewater after the successful micropollutants degradation, the hybridisation of semiconductor material with magnetic particles enables efficient photocatalyst recovery from post-process suspension with the assistance of an external magnetic field [25,26]. Previously, spinel ferrites with a formula of AFe$_2$O$_4$, where A is a transition or alkaline earth metallic cation (Mn, Zn, Co, Ni, or Mg), were applied for photocatalyst separation [27,28]. Among the various studied magnetic nanomaterials, MnFe$_2$O$_4$ nanoparticles have attracted great attention due to their low cost, high chemical stability, and non-toxicity [29]. Simultaneously, Mn and Fe ions may activate

peroxymonosulphate through an electron-transport strategy mediated by the variable-valence metal sites [30].

Therefore, in this study, TiO$_2$/MXene/MnFe$_2$O$_4$ composite was synthesised and applied for the photocatalytic degradation of the PhACs mixture under simulated solar light irradiation. To further increase the degradation efficiency of ibuprofen and carbamazepine, the photocatalytic process was combined with the PMS activation. MXene - Ti$_3$C$_2$ was used as a Ti precursor for anatase/rutile TiO$_2$ formation and co-catalyst, and MnFe$_2$O$_4$ particles embedded in the structure of TiO$_2$/Ti$_3$C$_2$ played a dual role of magnetic part providing easy separation after the purification process and activation of PMS, to produce •SO$_4^-$ radicals.

In the presence of transition metals (Fe, Cu, Mn, Co), PMS may effectively produce sulphate radicals with strong oxidation ability [31,32]. The sulphate radical (•SO$_4^-$) possesses a close or even higher redox potential of 2.5–3.1 V (vs. NHE) compared to hydroxyl radical (E$_0$ =1.8–2.8 V) [33,34]. Moreover, sulphate radicals have higher selectivity, longer half-life (30–40 μs), and could be activated in the broader pH range from 2 to 8 than •OH radicals [35]. The effect of PMS concentration, pH, and interfering ions on the efficiency of photocatalytic processes of CBZ and IBP mixture photodegradation was studied in detail. Furthermore, the trapping experiments with scavengers were performed to determine the major reactive species participating in the TiO$_2$/MXene/MnFe$_2$O$_4$/PMS degradation process. Finally, the composite stability and reusability were tested in subsequent cycles of PhACs photocatalytic degradation.

2. Experimental

2.1. Materials

The MAX phase compound – Ti$_3$AlC$_2$ was provided by Luoyang Tongrun Info Technology Co. (China). The hydrofluoric acid (ACS reagent, 48%), NH$_4$F (ACS reagent, ≥ 98.0%), MnCl$_2$ (≥99% trace metals basis), and FeCl$_3$·6 H$_2$O (ACS reagent, 97%) were purchased from Sigma Aldrich. HCl (35–38%) and NaOH (pure p.a.) were provided by Chempur (Poland). Carbamazepine (Certified Reference Material) and Ibuprofen (≥ 98% (GC)) for the photocatalytic degradation process were provided by Sigma Aldrich. Potassium peroxymonosulphate (OXONE) was provided by Sigma Aldrich. The reagents were used as received with no further purification. Scavengers: tert-butanol (anhydrous, 99.5%), isopropanol (anhydrous, 99.5%), p-benzoquinone (reagent grade, ≥ 98%), and ammonium oxalate monohydrate (ACS reagent, ≥ 99%) for trapping experiments and reagents for model seawater: CaCl$_2$ (anhydrous, powder, 99.99% trace metals basis), MgCl$_2$ (anhydrous, ≥98%), Na$_2$SO$_4$ (ACS reagent, ≥99.0%, anhydrous, powder), and NaCl (ACS reagent, ≥99.0%) were supplied by Sigma Aldrich. Acetonitrile (HPLC grade) and H$_3$PO$_4$ (85%, HPLC grade) were used to determine the concentration of CBZ and IBU by HPLC and were provided by Sigma Aldrich. Deionised water (DI) was used in all experiments.

2.2. Synthesis of MnFe$_2$O$_4$

The magnetic nanoparticles were prepared by dissolving in 100 cm^3 of deionised water (DI), FeCl$_3$·6 H$_2$O and MnCl$_2$ in the molar ratio of 2:1. Next, 0.5 M NaOH solution was added dropwise until the pH reached 10. The suspension was transferred into a Teflon-lined stainless steel reactor. The reaction was performed at 180 °C for 6 h. The resulting material was separated with a magnet, washed 3 times with DI water, and dried at 50 °C to dry mass.

2.3. Preparation of Ti$_3$C$_2$T$_x$ and TiO$_2$/Ti$_3$C$_2$

The Ti$_3$C$_2$T$_x$ was obtained by aluminium etching from MAX phase compound – Ti$_3$AlC$_2$. In a typical process, 10 g of Ti$_3$AlC$_2$ was added gradually to 100 cm^3 of 48% HF and mixed at room temperature for 24 h. Next, the material was centrifuged and washed with DI water until

neutral pH.

To prepare the TiO$_2$/Ti$_3$C$_2$ composite, 60 cm^3 of 3 M HCl was mixed with 0.1 g NH$_4$F. Next, 0.4 g of Ti$_3$C$_2$T$_x$ was added to the above mixture and sonicated for 10 min. Then the suspension was mixed for 30 min and transferred into a Teflon-lined stainless steel reactor. The reaction was performed at 220 °C for 24 h. The resulting material was washed several times with DI water and dried at 50 ℃ to dry mass.

2.4. Preparation of MnFe$_2$O$_4$/TiO$_2$/Ti$_3$C$_2$ composite

The composites with 5 wt% and 20 wt% of MnFe$_2$O$_4$ were prepared by ultrasonic-assisted self-assembly approach. In this regard, 0.5 g of TiO$_2$/Ti$_3$C$_2$ was dispersed in 50 cm^3 of water/ethanol mixture (1:4 v/v), while an appropriate amount of MnFe$_2$O$_4$ was dispersed similarly in 50 cm^3 of water/ethanol mixture (1:4 v/v), separately. Both suspensions were sonicated in the bath for 15 min. After that, MnFe$_2$O$_4$ dispersion was added dropwise to TiO$_2$/Ti$_3$C$_2$ suspension under sonication. As prepared material was mixed for 1 h using a mechanical stirrer. The prepared composite was separated with a magnet and washed 3 times with DI water. Finally, it was dried at 50 ℃ to dry mass.

2.5. Characterisation of as-obtained materials

The crystal structure of the samples was characterised by the powder X-ray diffraction method using the Rigaku Intelligent X-ray diffraction (XRD) system SmartLab (Rigaku Corporation, Tokyo, Japan). The diffractograms were obtained in a 2θ range of 5–80°, with a speed of 2°·min^{-1} and a step of 0.01°. The quantitative phase analysis was performed using the Rietveld refinement with X'Pert HighScore Plus.

Specific surface areas were estimated through the BET model (Brunauer-Emmett-Teller) at 77 K (boiling point of liquid nitrogen) with the Micromeritics Gemini V apparatus (model 2365) (Norcross, GA, USA). Samples were degassed under N$_2$ at 200 °C for 2 h before the measurements.

A ThermoScientific Evolution 220 spectrophotometer (Waltham, MA, USA) was used to record the UV–vis diffuse reflectance spectra (DRS). The measurements were performed in the wavelength range from 200 nm to 800 nm, using barium sulphate as a standard reference.

The morphologies of the synthesised materials were examined by scanning electron microscopy (SEM) using SEM Microscope FEI Quanta FEG 250. Transmission electron microscope (TEM) analyses were performed using (S)TEM Titan3 G2 60–300 with detector Super-X detector (Thermo Fisher Scientific).

A SQUID magnetometer (Quantum Design MPMS XL7) was employed to magnetically characterise the samples (room temperature hysteresis loops and magnetisation versus temperature, 10 −300 K).

The X-ray photoelectron spectroscopy (XPS) measurements were performed using Escalab 250Xi multispectroscope (ThermoFisher Scientific) with a monochromatic AlKα X-ray source. The high-resolution spectra were registered in the core-level binding energy range of Ti 2p, C 1 s, and O 1 s at pass energy of 20 eV.

The photoluminescence spectra (PL) were registered using a spectrofluorometer Shimadzu RF-6000 (Kyoto, Japan). As an excitation source, a 150 W Xenon lamp was used with an excitation wavelength of 300 nm.

The Fourier-transform infrared spectroscopy (FTIR) spectra were recorded using Nicolet iS10 FT-IR Spectrometer (Thermo Fisher Scientific Inc., MA, USA) in the transmittance mode in the wavenumber range from 400 to 4000 cm^{-1}.

Electrochemical impedance spectra were registered with potentiostat/galvanostat Metrohm Autolab PGSTAT204 in the range between 10^5 and 0.1 Hz with AC voltage amplitude equal to 0.01 V. Samples were placed on the carbon screen-printed electrode with Ag reference electrode. The electrolyte solution (0.5 M Na$_2$SO$_4$) was purged with argon for 10 min prior to the measurements. The Mott Schottky analysis was performed to determine the flat band (F$_b$) potential of the TiO$_2$/Ti$_3$C$_2$

composite and MnFe$_2$O$_4$. The EIS data were recorded from the anodic towards a cathodic direction for the applied frequency of 1000 Hz in the potential range from 0 to − 1.8 V. Transient photocurrent response of photocatalysts was recorded at the light on/off interval equal 25 s at 0 V vs. Ag under 372 nm LED light illumination.

Thermogravimetric analysis (TGA) was performed using a thermogravimetric analyser 2 SF/1100 from Mettler Toledo. The conditions of the measurement were: airflow 10 cm^3/min, temperature range: 25–750 °C, heating rate 10 °C/min.

ICP-OES measurement was performed based on the Polish Standard PN-EN-ISO-11885_2009E. Iron Photmetric Test Kit (0.01–1 mg/dm^3) and spectrophotometer DR5000 (HACH LANGE) with a wavelength of 485 nm were used to determine iron content in the post-process solution.

2.6. Photocatalytic degradation analyses

Typically, 0.05 g of the photocatalyst was dispersed in 25 cm^3 of the mixture of carbamazepine (7 mg/dm^3) and ibuprofen (10 mg/dm^3) solution (pH 6.7, initial TOC value of 13.3 mg/dm^3). The photocatalytic experiment was performed in a 25 cm^3 reactor with a quartz window equipped with an airflow. As a light source, imitating the sunlight spectrum, a 300 W Xe lamp (LOT Oriel, Darmstadt, Germany) with a light flux in the UV range (310 nm $< \lambda <$ 380 nm) equalled 35 mW·cm^{-2} was operated. Before irradiation, the photocatalyst suspension was kept in the dark for 30 min to reach adsorption-desorption equilibrium. During the photodegradation process, 1 cm^3 of the suspension was collected at 0, 20, 40, and 60 min and separated using a 0.2 μm syringe filter. The rate of pharmaceutical degradation was controlled using reverse-phase high-performance liquid chromatography (Shimadzu UFLC LC-20AD (Kyoto, Japan) with a photodiode array detector (Shimadzu SPD-M20A). The analyses were performed at 45 °C and under isocratic flow conditions of 1.5 cm^3·min^{-1} for carbamazepine and 0.5 cm^3·min^{-1} for ibuprofen. A volume composition of the mobile phase of 70% acetonitrile, 29.5% water, and 0.5% orthophosphoric acid was used to determine ibuprofen concentration, while 60% water, 39.5% acetonitrile, and 0.5% orthophosphoric acid to determine carbamazepine concentration. The change in total organic carbon (TOC) during the photocatalytic process was analysed using a Shimadzu TOC analyser.

Further experiments were performed with the addition of PMS to the suspension (concentration in CBZ/IBU solution equal to 0.0625 mM, 0.125 mM, or 0.25 mM). After the addition of PMS (0.25 mM), the initial pH of the solution decreased to 5.2. The samples (1 cm^3) were collected and filtrated during the photocatalytic process, and after that 200 μL of methanol was added to quench the radical species.

Further analyses were conducted in the model seawater to evaluate the effect of interfering ions on the efficiency of photocatalytic processes of CBZ and IBP mixture removal. The model seawater contained 2.5% NaCl, 1.1% MgCl$_2$, 0.4% Na$_2$SO$_4$, and 0.16% CaCl$_2$ in DI water. Moreover, the effect of the solution pH was investigated. The solution pH was adjusted with 0.1 M HCl or 0.1 M NaOH to values 4.5 and 9.5, respectively.

The radical trapping experiments were carried out under the same conditions in the presence of scavengers (with a concentration equal to the 10-fold concentration of contaminant). Ammonium oxalate (AO) was applied as a hole scavenger (h$^+$), tert-butanol (t-But) for free hydroxyl radicals (•OH), isopropanol (iPr) for hydroxyl radicals and sulphate radicals (•OH and •SO$_4^-$) and p-benzoquinone (BQ) for superoxide radical anions (•O$_2$) scavenging test.

In order to evaluate the stability and recyclability of the photocatalyst/PMS system, after each process, the photocatalyst was separated from the solution, and a fresh portion of the pharmaceuticals mixture was poured with the addition of PMS. The photocatalyst was used without any additional treatment. The photocatalytic performance was evaluated within four subsequent cycles under the same reaction conditions.

3. Results and discussion

3.1. Characterization of $MnFe_2O_4$, TiO_2/Ti_3C_2 and $TiO_2/Ti_3C_2/MnFe_2O_4$ photocatalysts

The XRD patterns of Ti_3AlC_2 and $Ti_3C_2T_x$ after Al etching are presented in Fig. 1a. The presence of diffraction signals at $2\Theta = 8.9°$, $18.2°$, and $27.5°$ corresponding to (002), (004), and (006) planes confirmed the successful formation of MXene. Moreover, the XRD analysis was used to determine the phase composition of the $MnFe_2O_4$, TiO_2/Ti_3C_2, and $TiO_2/Ti_3C_2/MnFe_2O_4$, as shown in Fig. 1b. The diffraction signals of $MnFe_2O_4$ are assigned to the (220), (311), (400), (422), (511), (440) planes at $29.8°$, $34.8°$, $42.7°$, $52.8°$, $56.3°$, and $61.9°$ 2Θ. Diffractogram of TiO_2/Ti_3C_2 includes signals assigned to anatase (101), (004), (200), (211), (204), (116) planes at $25.2°$, $37.7°$, $47.9°$, $55.0°$, $62.6°$, $68.8°$, and rutile (110), (101), (111), (210), (211), (220) planes at $27.3°$, $36.0°$, $41.1°$, $43.9°$, $54.2°$, $56.4°$, respectively. In the XRD pattern of the composite material, signals for anatase, rutile, and $MnFe_2O_4$ were observed. No other signals were noticed, which confirmed the phase-pure crystallographic structure of the obtained photocatalyst. This result also demonstrates that the $MnFe_2O_4$ was successfully combined with TiO_2/Ti_3C_2. The phase distributions (percentage, wt%, of each phase) of prepared materials are listed in Table 1. Based on the Rietveld refinement, the content of the magnetic part ($MnFe_2O_4$) was about 4% for $TiO_2/Ti_3C_2/5\%MnFe_2O_4$ and 17% for $TiO_2/Ti_3C_2/5\%MnFe_2O_4$ composites. However, no signals corresponding to MXene - Ti_3C_2 were observed, probably due to the low content or well dispersion [36,37].

Therefore, to verify the presence of Ti_3C_2 in the composite after solvothermal synthesis, the XPS analysis was performed, and the results are presented in Fig. 2. The survey spectrum is presented in Fig. S2 in the Supporting Materials. The characteristic weak signals for MXene Ti-C and Ti^{3+} bonds (454.5 eV and 457.4 eV) indicated the presence of a small amount of Ti_3C_2. The most intense signal of Ti^{4+} (459 eV) confirmed that the material was almost entirely oxidised to TiO_2 [38, 39].

The C1s spectrum was deconvoluted for five peaks corresponding to Ti-C (283 eV), C-Ti-O (283.5 eV), adventitious carbon (285 eV), C-O (286.7 eV), and C-F bonds (288.5 eV). The O 1 s spectrum confirmed the presence of Ti-OH (528.5 eV) bonds and Ti-O (530 eV), as well as C=O (531.5 eV) and C-O (532.5 eV).

Furthermore, the thermogravimetric (TGA) analysis was performed to confirm the existence of Ti_3C_2 in the composite material. As can be seen in Fig. 3, the 0.7% weight gain from 250 °C to 400 °C was noticed. This change was related to the oxidation of MXene layers to form anatase.

Table 1
The phase compositions of the samples based on Rietveld refinement.

Sample	Anatase (%)	Rutile (%)	$MnFe_2O_4$ (%)
$MnFe_2O_4$	-	-	100
TiO_2/Ti_3C_2	40	60	-
$TiO_2/Ti_3C_2/5\%MnFe_2O_4$	38	58	4
$TiO_2/Ti_3C_2/20\%MnFe_2O_4$	32	51	17

The ICP-OES and SEM-EDS analyses for $TiO_2/Ti_3C_2/5\%MnFe_2O_4$ sample presented in Table S1 and Fig. S1 in the Supporting Materials confirmed the presence of Ti, Mn and Fe in the composite structure and correlated well with XRD, XPS and TGA analyses results.

The optical properties were characterised by DR/UV–vis, as presented in Fig. 4. The TiO_2/Ti_3C_2 exhibited strong absorption in the UV range with a threshold of about 420 nm. The light absorption in the range above 450 nm resulted from the presence of titanium carbide, which absorbs light within the whole light range [40]. Bandgap energy (E_g) values were calculated according to the Kubelka-Munk function, $(R)^n \cdot E_{ph}^n$ against E_{ph}, where E_{ph} is photon energy, while n has values of $n = 2$ and $1/2$ for indirect ($MnFe_2O_4$) and direct (TiO_2) transition, respectively. The plots are presented in Fig. S3 in the Supporting Material. Furthermore, the estimated E_g values are summarised in Table 2. The manganese ferrite particles exhibited the lowest E_g value of 1.5 eV, which agrees with the literature [41].

The narrow bandgap of TiO_2/Ti_3C_2 resulted from the presence of rutile in the composite structure. Furthermore, the specific surface areas of the photocatalytic materials are presented in Table 2. It can be observed that both components and composite materials possess similar surface areas in the range of 12–13 m^2/g.

The SEM images of TiO_2/Ti_3C_2, $MnFe_2O_4$, and $TiO_2/Ti_3C_2/MnFe_2O_4$ composites are presented in Fig. 5. The TiO_2/Ti_3C_2 composite contained a mixture of various size decahedral and octahedral TiO_2 particles, exposing { 1 0 1} and { 0 0 1} facets. The morphology of the $MnFe_2O_4$ had a spherical shape (average diameter $\sim$ 80 nm) with the presence of the agglomerates, ascribed to relatively stronger interaction among magnetic particles [42].

Furthermore, the TEM analysis was performed to characterise the morphology and microstructure of $TiO_2/Ti_3C_2/5\%MnFe_2O_4$, and the images are shown in Fig. 6. The presence of anatase, rutile, Ti_3C_2, and $MnFe_2O_4$ was noticed. In the corresponding HRTEM image, the d-spacing was $\sim$0.258 nm and $\sim$0.482 nm, respectively, which corresponded to the (111) and (311) planes of $MnFe_2O_4$. For anatase, d-spacing of $\sim$0.351 nm was assigned to the (101) planes, while for rutile, $\sim$0.215 nm and $\sim$0.323 nm were assigned to the (111) and (110)
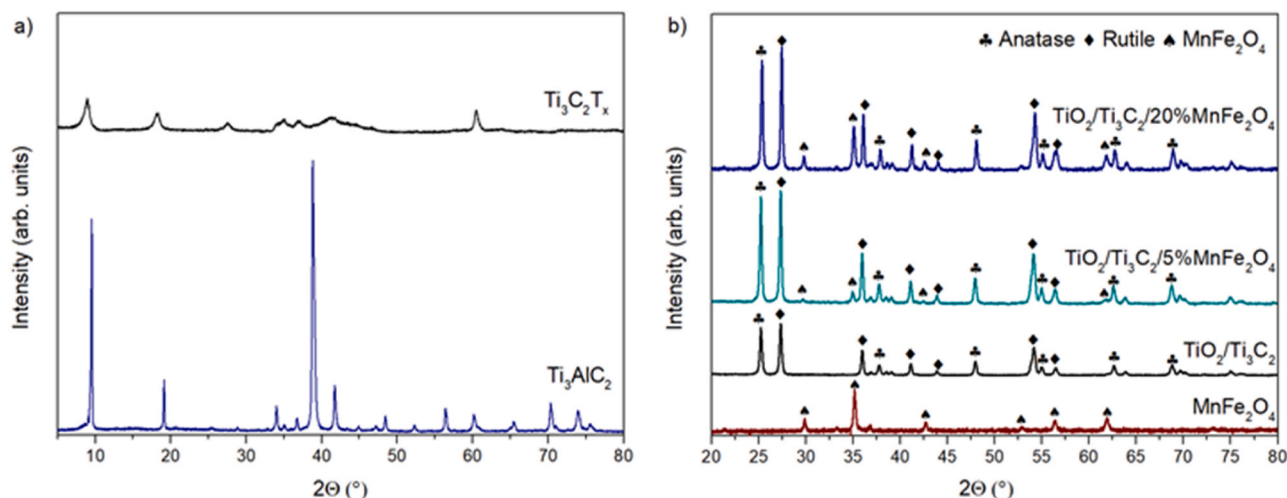

Fig. 1. The XRD diffractograms for Ti_3AlC_2 and $Ti_3C_2T_x$ (a) and prepared materials (b).

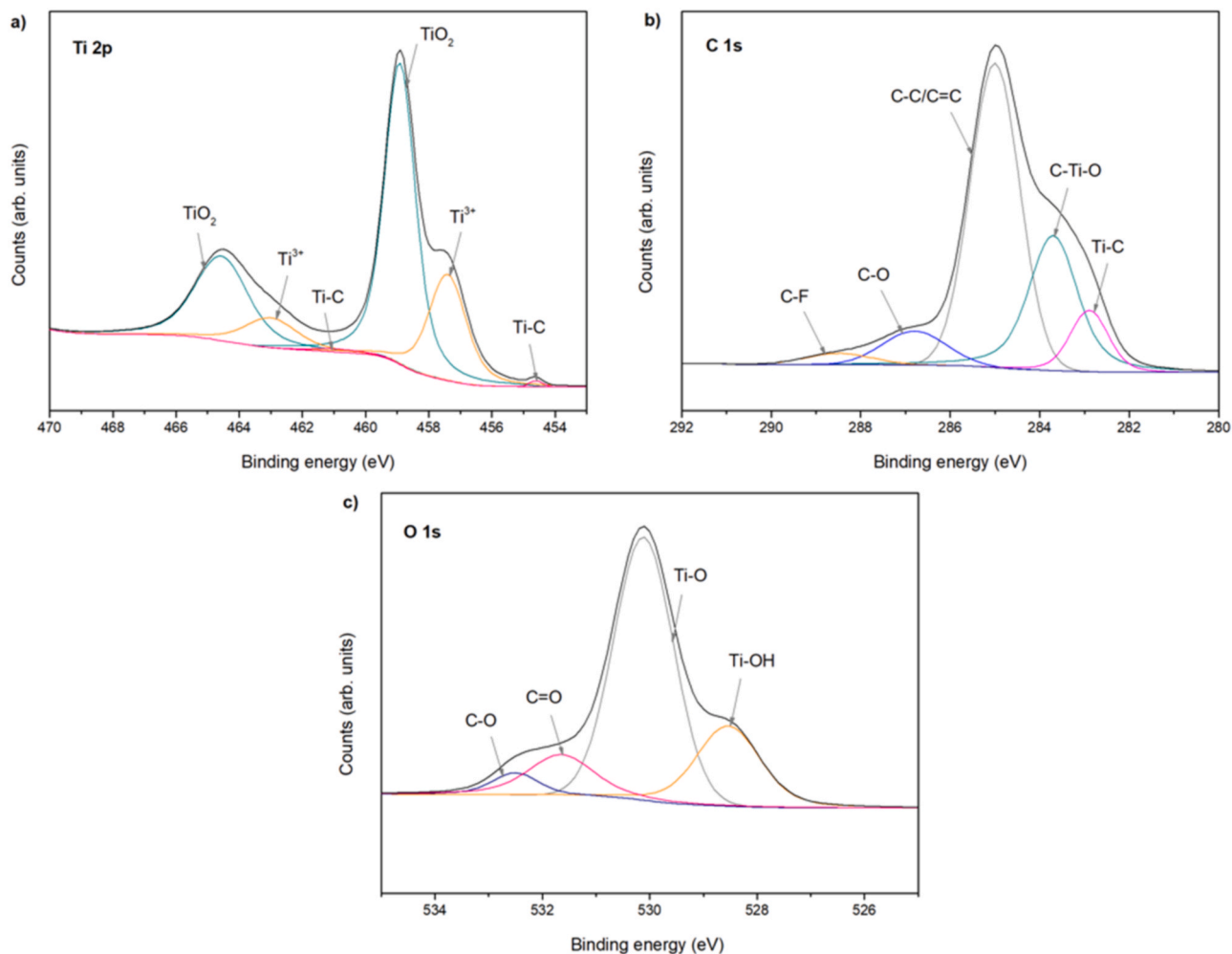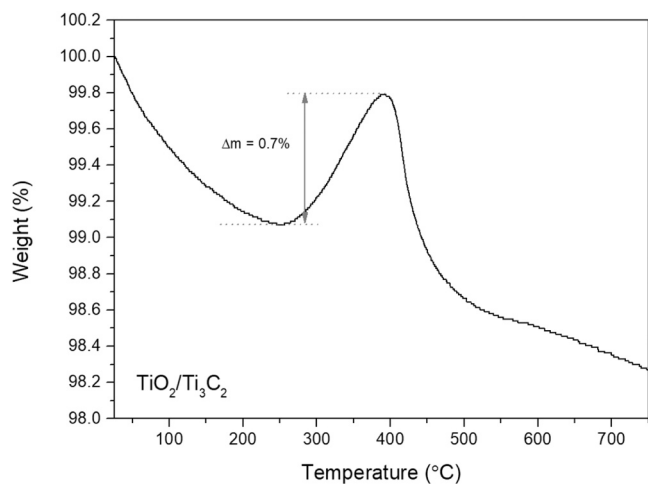**Fig. 2.** XPS spectra for Ti 2p (a), C 1 s (b) and O 1 s (c) regions for TiO_2/Ti_3C_2 composite.
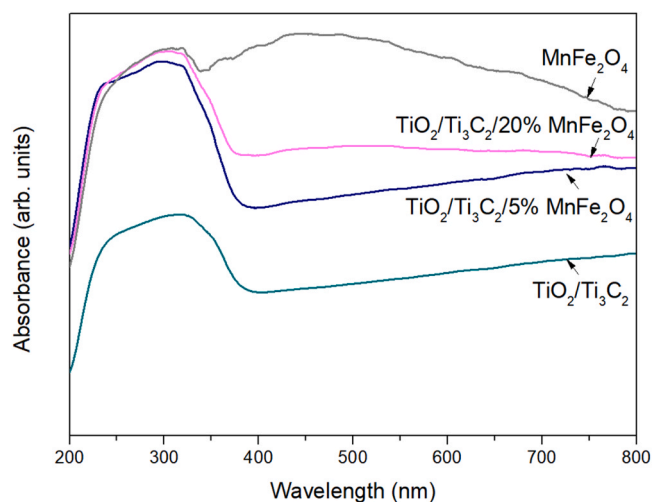

Fig. 3. TG curve of TiO_2/Ti_3C_2.

Fig. 4. The DR/UV–vis spectra for prepared materials.

planes, respectively [43]. STEM-EDS elemental mapping proved that $MnFe_2O_4$ particles were uniformly distributed in the composite material with some agglomerates (see Fig. 6 and Fig. S4 in the Supporting Materials).

The photoluminescence spectra of TiO_2/Ti_3C_2 and $TiO_2/Ti_3C_2/5\%$ $MnFe_2O_4$ were analysed under an excitation of 300 nm (Fig. 7). The materials showed a broad visible emission band between 400 and 700 nm with a maximum of 465 nm associated with the multi-photon process occurring due to the participation of various electronic states within the band gap. Both spectra are similar and broad with no clear shift. Only, a slight decrease in the photoluminescence intensity for $TiO_2/Ti_3C_2/MnFe_2O_4$ composites, compared with TiO_2/Ti_3C_2 was

Table 2
BET surface area and calculated bandgap energy for prepared materials.

Sample	BET surface area (m^2/g)	E_g (eV)
$MnFe_2O_4$	13.4	1.5
TiO_2/Ti_3C_2	12.5	3.0
$TiO_2/Ti_3C_2/5\%MnFe_2O_4$	12.9	2.99
$TiO_2/Ti_3C_2/20\%MnFe_2O_4$	12.1	3.05

noticed.

Furthermore, the Gaussian fitting and deconvolution of PL spectra for $TiO_2/Ti_3C_2/5\%MnFe_2O_4$ are shown in Fig. 8. The deconvolution of the spectrum reveals ten components centered at 425 nm, 443 nm, 465 nm 482 nm, 492 nm, 516 nm, 573 nm, 639 nm, 692 nm, and 732 nm. The first band (violet-blue) at 425 nm may be attributed to the self-trapped excitons of TiO_6 octahedra [44]. The bands in the blue and green region may correspond to the shallow trap due to the Ti^{3+} states just below the conduction band and singly ionised oxygen vacancies, respectively. The band at 573 nm may be ascribed to intrinsic defects or the recombination of electrons and holes on the amorphous carbon of MXene [44,45]. The orange-red region emission may be assigned to surface oxygen and hydroxyl species [44] There is no significant difference in the deconvolution of pure TiO_2/Ti_3C_2 and $TiO_2/$-$Ti_3C_2/MnFe_2O_4$ composites (Fig. S5 in the Supporting Materials). For $MnFe_2O_4$ very weak emission was observed. Characteristic blue emission may be attributed to the radiative defects related to the interface traps existing at the grain boundaries. Green emissions may correspond to oxygen vacancies [46]. The yellow-orange signal may be related to the Mn d-d emission [47].

Fig. 9 shows the room temperature hysteresis loops (magnetisation, M, versus applied magnetic field, m_0H) of pure $MnFe_2O_4$ and $TiO_2/$$Ti_3C_2/MnFe_2O_4$ composites. Pure $MnFe_2O_4$ had the highest saturation magnetisation of 68 emu/g. Meanwhile, the magnetic properties of the composite were reduced in comparison to $MnFe_2O_4$ to about 12 emu/g for $TiO_2/Ti_3C_2/20\%$ $MnFe_2O_4$ and 5 emu/g for $TiO_2/Ti_3C_2/5\%$ $MnFe_2O_4$, as a consequence of the presence of a relatively high fraction of non-magnetic component of TiO_2/Ti_3C_2. Nevertheless, the coercive field, H_c, is not significantly modified after the preparation of the final composites (see inset of Figure 8, H_c 60 Oe in the three samples). It is important to notice that, as can be seen in the image in Fig. 8, even the sample with the lowest magnetic component ($TiO_2/Ti_3C_2/5\%$ $MnFe_2O_4$) can be effectively separated from the liquid using a magnet bar and thus possess good properties for recovery and recycling.

The magnetic response of the samples was further analysed through the temperature dependence of the magnetisation. Fig. 10a shows M versus temperature at the applied magnetic field of 6 T for the manganese ferrite and the TiO_2/Ti_3C_2 composites. As concluded from the hysteresis loops, an overall reduction in M is found in the composites due to the non-magnetic nature of TiO_2/Ti_3C_2. However, if the magnetic response of this component is analysed in further detail under similar experimental conditions (see inset of Fig. 10a), negative magnetisation is found to be linked to its diamagnetic nature. Such a negative contribution (low in absolute value) would not contribute significantly to the net magnetisation. Anyway, the magnetisation was estimated considering the magnetic contribution of each component, that is, $M_{composite}$ = (%) * $M_{MnFe2O4}$ + (1 - %)* $M_{TiO2/Ti3C2}$, considering % from the Rietveld refinement (4% and 17%, see Table 1). As shown in Fig. 10a, a close
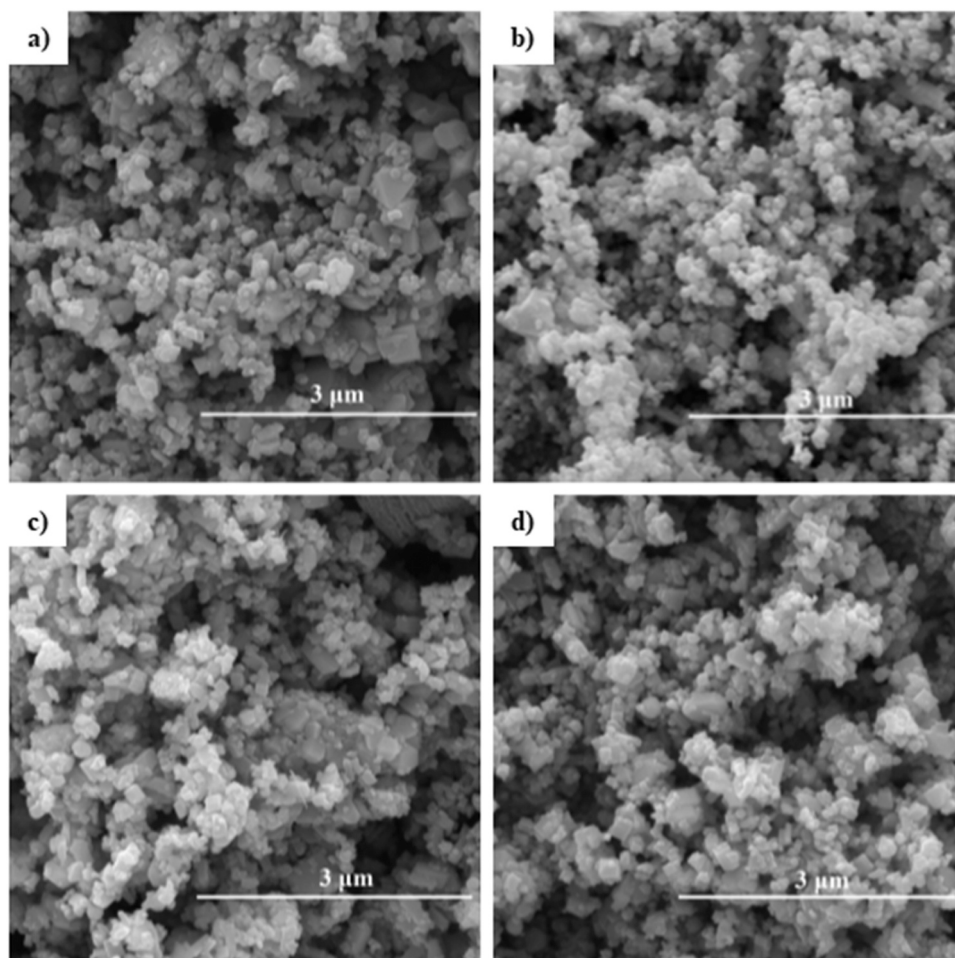

Fig. 5. The SEM image of pure $MnFe_2O_4$ (a), TiO_2/Ti_3C_2 (b), $TiO_2/Ti_3C_2/5\%MnFe_2O_4$ (c), $TiO_2/Ti_3C_2/20\%MnFe_2O_4$ (d).

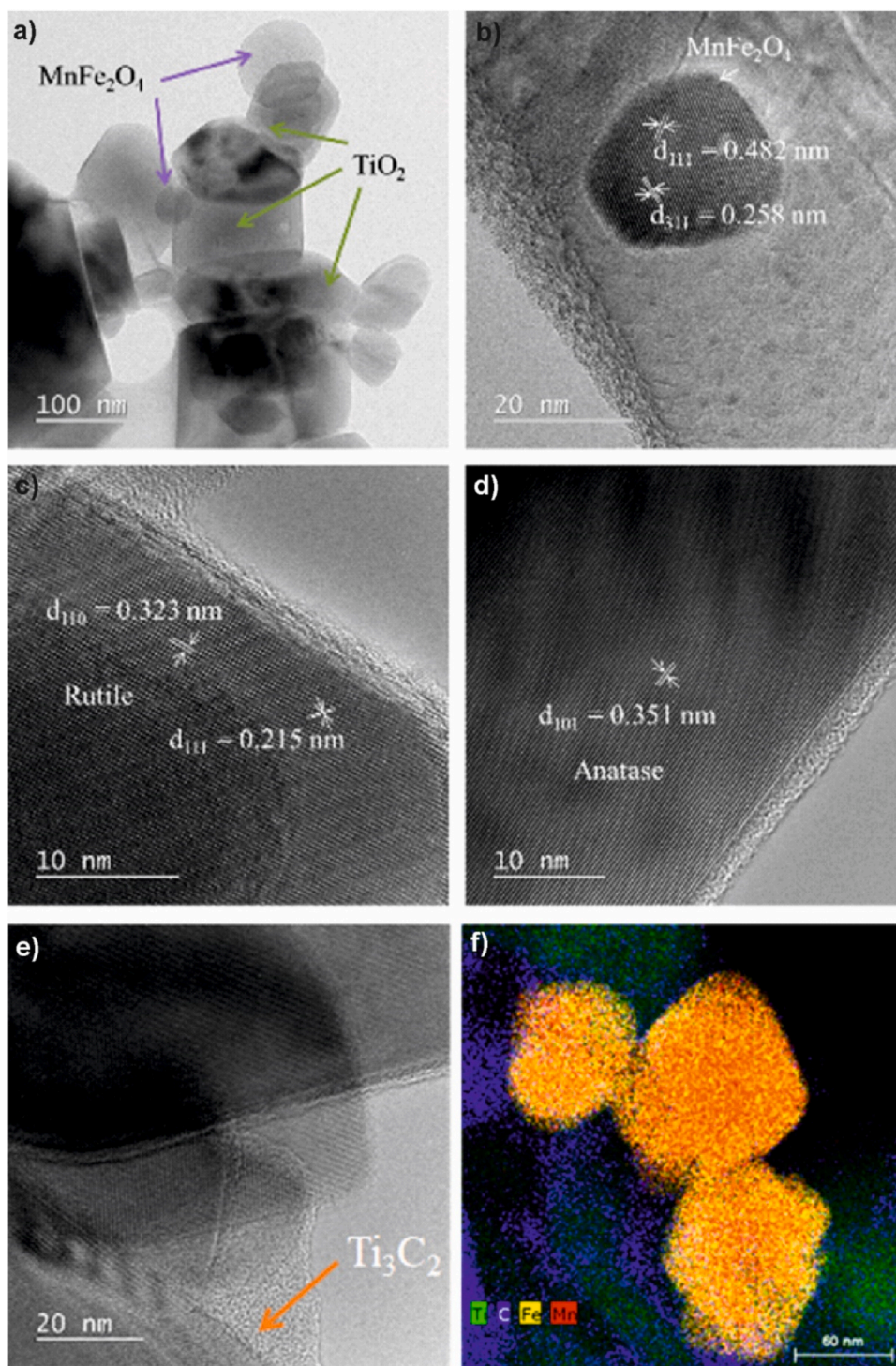**Fig. 6.** The TEM image of $TiO_2/Ti_3C_2/5\%MnFe_2O_4$ (a), HRTEM with marked lattice spacing for $MnFe_2O_4$ (b), rutile (c) and anatase (d), TEM image for Ti_3C_2 (e), STEM-EDS elemental mapping of $TiO_2/Ti_3C_2/5\%MnFe_2O_4$ (f).

agreement between this estimation (line) and the experimental magnetisation (symbols) is found. Finally, regarding the magnetic characterisation, the Zero-Field-Cooled (ZFC)-Field-Cooled (FC) magnetisation curves are displayed in Fig. 10b for the three analysed samples, where the magnetisation for the composites is normalised (M/%) to comparatively analyse their magnetic response. Typical curves of superparamagnetic nanoparticles with Blocking temperatures slightly above room temperature are obtained in all the samples. The proximity of the Blocking temperature to the operation temperature (300 K) guarantees an optimum magnetic behaviour of the magnetic composites in aqueous

dispersions, that is, low Hc and magnetisation at the remanence to avoid magnetic interparticle interactions and high magnetic susceptibility to allow and efficient recovery through the action of an external magnetic field.

The EIS Nyquist plots are shown in Fig. 11a. It can be seen that $TiO_2/Ti_3C_2/5\%\ MnFe_2O_4$ showed the minimum radius of arc in comparison to other samples, which suggests that coupling between TiO_2/Ti_3C_2 and 5% of $MnFe_2O_4$ decreased the charge-transfer resistance. As shown in Fig. 11b, all samples present a stable photocurrent within 5 on/off cycles, indicating that these materials can be excited to generate
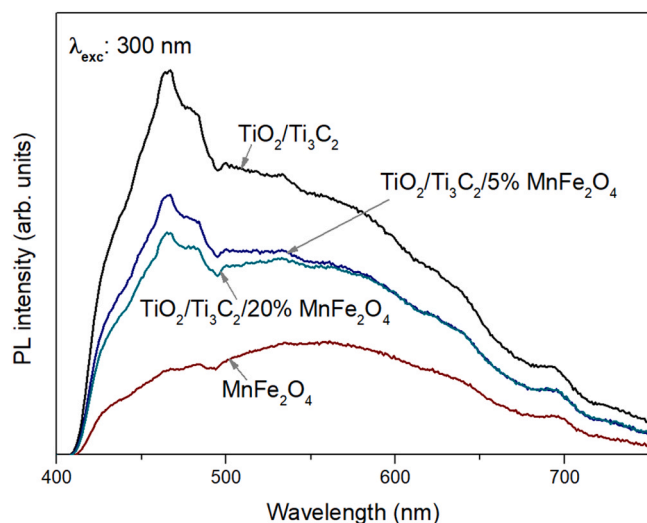
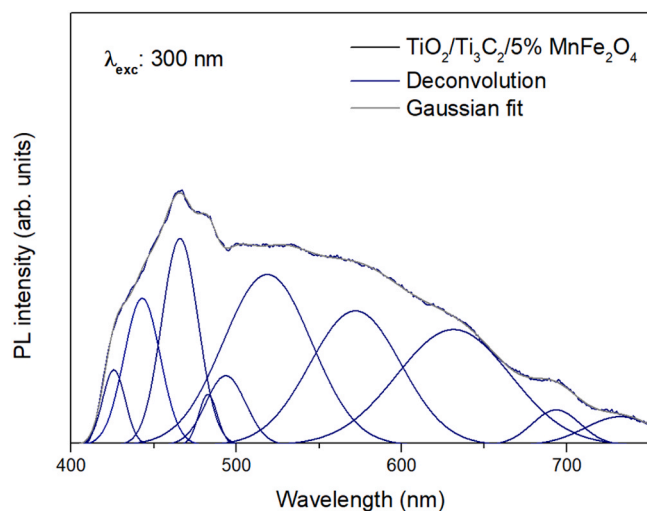**Fig. 7.** The PL spectra of the prepared materials.

Fig. 8. The Gaussian fitting and deconvolution of PL spectra of the $TiO_2/Ti_3C_2/$ 5%$MnFe_2O_4$.
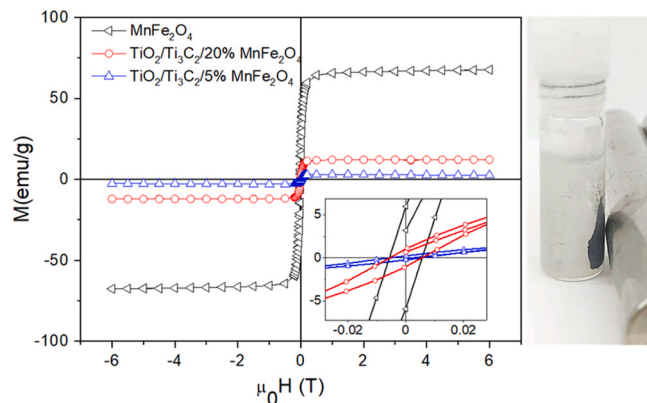

Fig. 9. Room temperature hysteresis loops for pure $MnFe_2O_4$ and composites. Inset: enlargement of the low field region.

electron–hole pairs. However, for pure $MnFe_2O_4$ the photocurrent response is very weak, which is related to the low number of generated charge carriers. For $TiO_2/Ti_3C_2/5\%$ $MnFe_2O_4$, slightly higher photocurrent density was observed than TiO_2/Ti_3C_2, suggesting efficient transfer and improved electron-hole separation.

According to the slope of Mott Schottky plots (Fig. 12), both $TiO_2/$ Ti_3C_2 and $MnFe_2O_4$ presented n-type semiconductor characteristics. The potential of TiO_2/Ti_3C_2 and $MnFe_2O_4$ flat band edge position, which for n-type semiconductors is almost equal to the conduction band potential, were recorded at -1.21 and -1.4 vs Ag. These values were converted to a value of -0.41 V and -0.62 V vs. NHE. Considering the bandgap value for TiO_2/Ti_3C_2 and $MnFe_2O_4$ equal to 3.0 eV and 1.5 eV, respectively, the valence band edge position were calculated as 2.59 V and 0.88 V vs. NHE.

3.2. Photocatalytic activity in reaction of ibuprofen and carbamazepine degradation

Firstly, the photolysis of ibuprofen and carbamazepine was analysed to notice the differences between processes with or without photocatalyst and verify the effect of PMS addition. As shown in Fig. 13, the photolysis of CBZ reached 23% within 60 min, while for IBP 49% within 60 min under simulated solar light irradiation. In these cases, the mineralisation measured as TOC reduction was not observed. After the addition of PMS (0.25 mM), the degradation for both pharmaceuticals increased to about 90% within 60 min. Nevertheless, the TOC concentration did not decrease.

The efficiency of carbamazepine and ibuprofen photodegradation for composite materials is presented in Fig. 14. The photocatalytic activity of pure $MnFe_2O_4$ was inefficient, which confirmed that although the lowest band gap, magnetic material did not show the ability for photodegradation and could only absorb a low amount of CBZ and IBP in the dark reaction (see Fig. S6 in the Supporting Materials). This may be explained by the fast recombination of electron-hole pairs [48]. Based on XRD analysis, the TiO_2/Ti_3C_2 composite sample contained TiO_2 as a mixture of anatase and rutile. Therefore due to the difference in the position of band gaps, the formation of heterojunction in TiO_2 material can be noticed. According to our previous work [22] focusing on the influence of the solvothermal reaction environment on morphology and photocatalytic activity, it was found that at the same hydrothermal reaction time and temperature, higher activity in reaction of acetaminophen degradation revealed sample obtained in NH_4F/HCl solution consisting of anatase and rutile combined with trace amounts of Ti_3C_2 compared to the sample of anatase modified with Ti_3C_2 prepared in HBF_4/H_2O solution. The direct contact between these two crystalline TiO_2 polymorphs may facilitate the interparticle transfer of the photogenerated charges in the photocatalytic processes and improve the photocatalytic activity [49–51]. The introduction of 5 wt% of manganese ferrite into the TiO_2/Ti_3C_2 photocatalyst structure did not affect the degradation efficiency of both pharmaceuticals, which reached 100% after 60 min of irradiation. However, the incorporation of a higher amount of $MnFe_2O_4$ (20%) significantly decreased the photocatalytic activity. This phenomenon may be attributed to the excessive amount of magnetic light diffusing particles that may hinder the contact between the photocatalyst and the light or become a new electron-hole recombination centre, which reduces the lifetime of the photogenerated charge carriers [52,53].

The TOC reduction efficiency during the photodegradation process is presented in Fig. 15. For TiO_2/Ti_3C_2 and $TiO_2/Ti_3C_2/5\%$ $MnFe_2O_4$ composite, the mineralisation efficiency was about 40% within 60 min of irradiation. In the case of $TiO_2/Ti_3C_2/20\%$ $MnFe_2O_4$ composite and $MnFe_2O_4$, the mineralisation was not observed.

Furthermore, as presented in Fig. 16, the addition of PMS resulted in a significant increase in the degradation of both pharmaceuticals. Moreover, the combination of the photocatalytic degradation process for sample $TiO_2/Ti_3C_2/5\%MnFe_2O_4$ with PMS activation led to superior
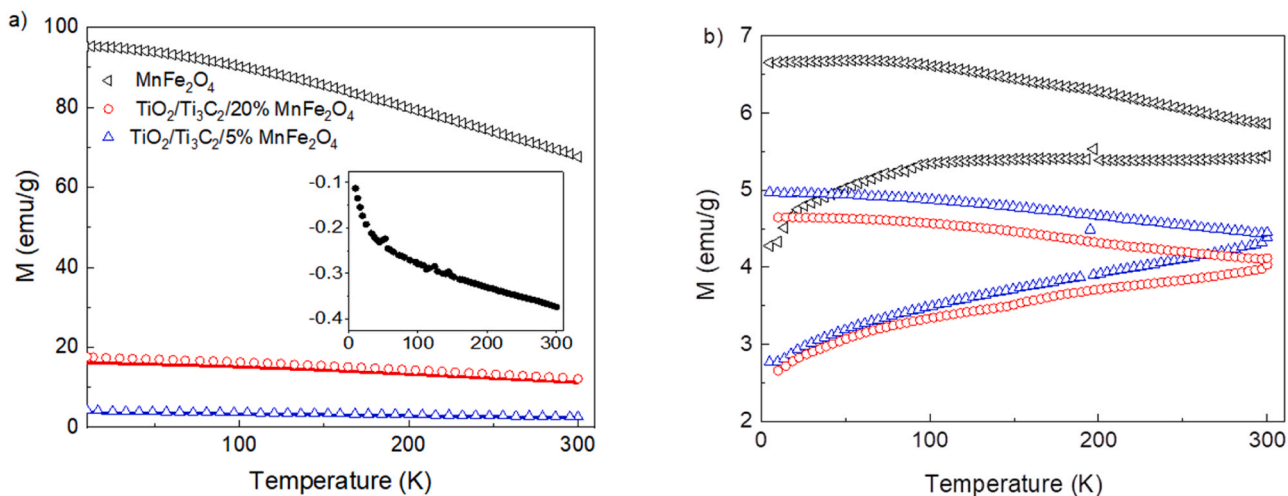
Fig. 10. High field magnetisation, M, (applied magnetic field $m_0H = 6$ T) for $MnFe_2O_4$ and prepared magnetic composites (a). Inset: M versus T at 6 T for the TiO_2/Ti_3C_2 component) and ZFC-FC magnetization curves for $MnFe_2O_4$ the prepared samples (applied magnetic field H = 50 Oe). M values for the composites were normalised to the relative fraction (%) (b).
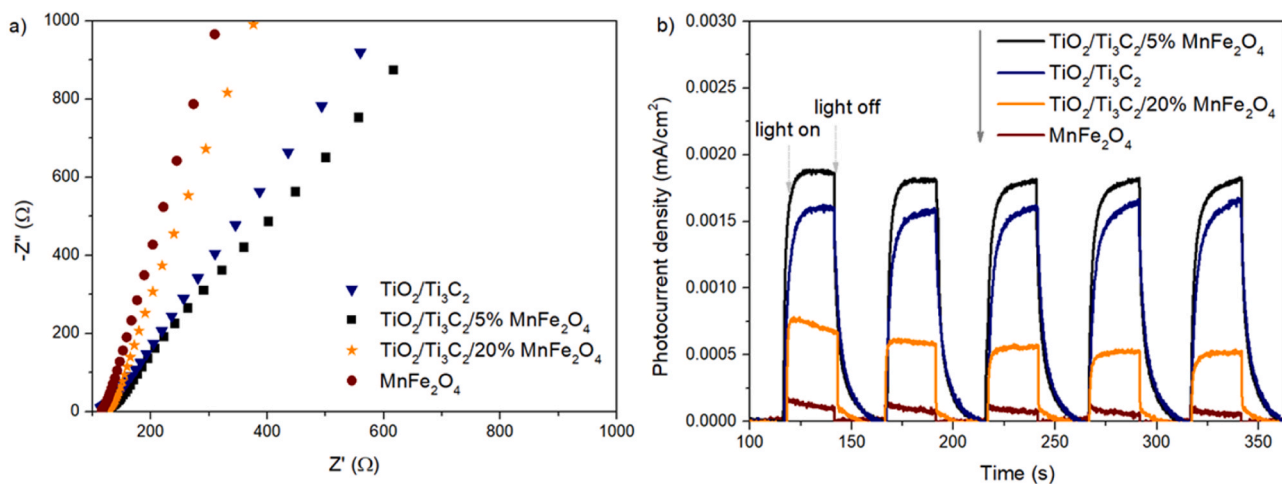

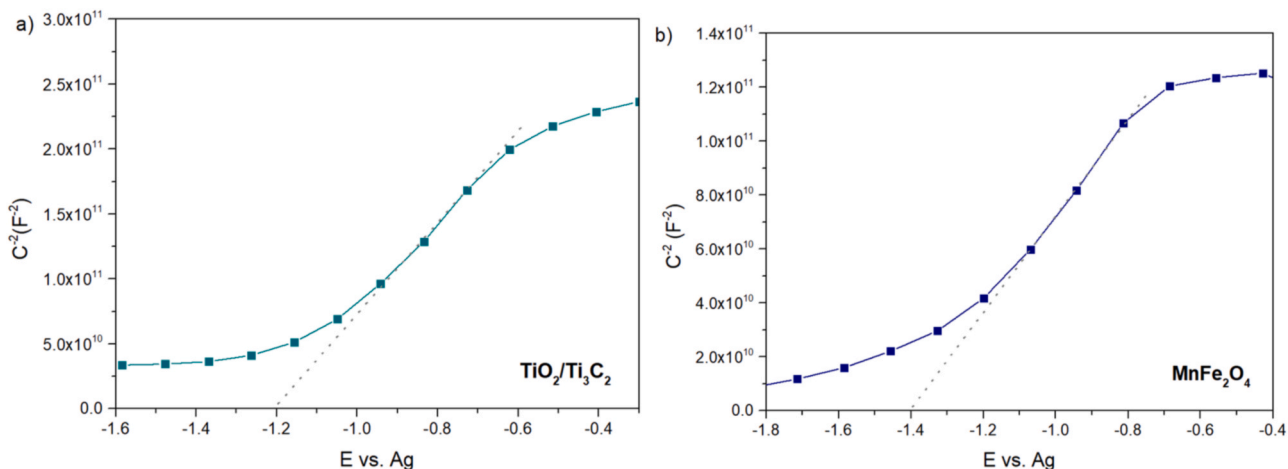**Fig. 11.** The EIS Nyquist plots (a) and generated photocurrent (b) for prepared materials.

Fig. 12. The Mott Schottky plots for TiO_2/Ti_3C_2 (a) and $MnFe_2O_4$ (b).
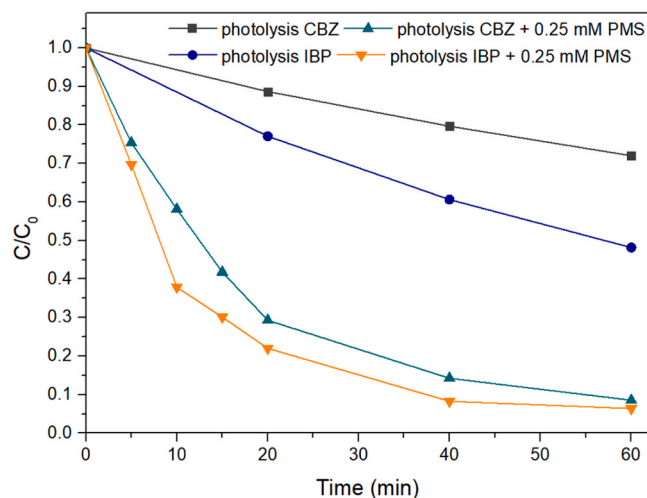
Fig. 13. The efficiency of carbamazepine and ibuprofen degradation in the CBZ/IBP mixture for photolysis and photolysis with PMS (0.25 mM).

photodegradation of the pharmaceutical mixture. In the case of the MnFe$_2$O$_4$, both Mn and Fe may activate PMS to produce sulphate radicals [54]. The effect of PMS concentration in the range of 0.065–0.25 mM for IBU and CBZ degradation and mineralisation was observed (see Figs. 16–17). The degradation rate was promoted with the increased concentration of the PMS. It can be explained by the fact that more PMS as a source of active species may improve pharmaceuticals degradation [55]. However, above a certain concentration, •SO$_4^-$ might be consumed by the excess PMS and produce less active SO$_5^{•-}$ [56]. Therefore, the highest degradation efficiency was observed for TiO$_2$/-Ti$_3$C$_2$/5%MnFe$_2$O$_4$ photocatalytic process combined with the activation of PMS with a concentration of 0.25 mM. After 20 min and 10 min of the advanced treatment process, 100% of CBZ and IBP were degraded, respectively.

Furthermore, a mineralisation efficiency measured as a TOC reduction was also improved for the sample TiO$_2$/Ti$_3$C$_2$/5% MnFe$_2$O$_4$/PMS compared to the sample without PMS (Fig. 17). The rate constant increased from 8.9 ± 0.27 min^{-1}·10^{-2} to 28.6 ± 0.98 ·10^{-2} min^{-1} for CBZ, and from 7.0 ± 0.18·10^{-2} min^{-1} to 53.0 ± 1.4 min^{-1}·10^{-2}, after the introduction of PMS into the reaction environment (Table S2 in the Supporting Materials). Therefore, the synergetic effect on the CBZ and IBP mixture degradation efficiency for peroxymonosulphate-assisted photocatalytic degradation over TiO$_2$/Ti$_3$C$_2$/5% MnFe$_2$O$_4$ photocatalyst was noticed.

The amount of the photocatalyst is another important factor determining the photocatalytic activity. The amount of TiO$_2$/Ti$_3$C$_2$/5% MnFe$_2$O$_4$ photocatalyst ranged from 0.5 to 2 g·dm^{-3}, with PMS concentration equal to 0.25 mM. As presented in Fig. 18, the highest degradation efficiency was observed for 2 g·dm^{-3}. However, the reduction of photocatalyst amount to 0.5 g·dm^{-3} enables degradation above 90% of CBZ and near 100% of IBP within 20 min of irradiation and TOC reduction of about 47%. The TOC removal was summarised in Table S3 in the Supporting Materials.

The effect of pH on the CBZ/IBP degradation was investigated at constant photocatalyst amount (2g·dm^{-3}) and PMS concentration (0.25 mM) by adjusting the initial pH of the solution. As shown in Fig. 19, a decrease in CBZ degradation can be noticed at a pH of 6.7 compared to 4.5, whereas the photodegradation efficiency of IBU was efficient at both pH values. However, increasing pH to 9.5 resulted in markedly decreased degradation of CBZ and IBP. The TOC removal was summarised in Table S3 in the Supporting Materials. Similarly, the lowest mineralisation efficiency of IBU and CBZ was observed under alkaline conditions, in which PMS may undergo self-decomposing without the production of reactive species. Moreover, in alkaline conditions, standard redox potentials of sulfate and hydroxyl radicals are lower as well as their lifetimes are shorter than in acidic conditions [57,

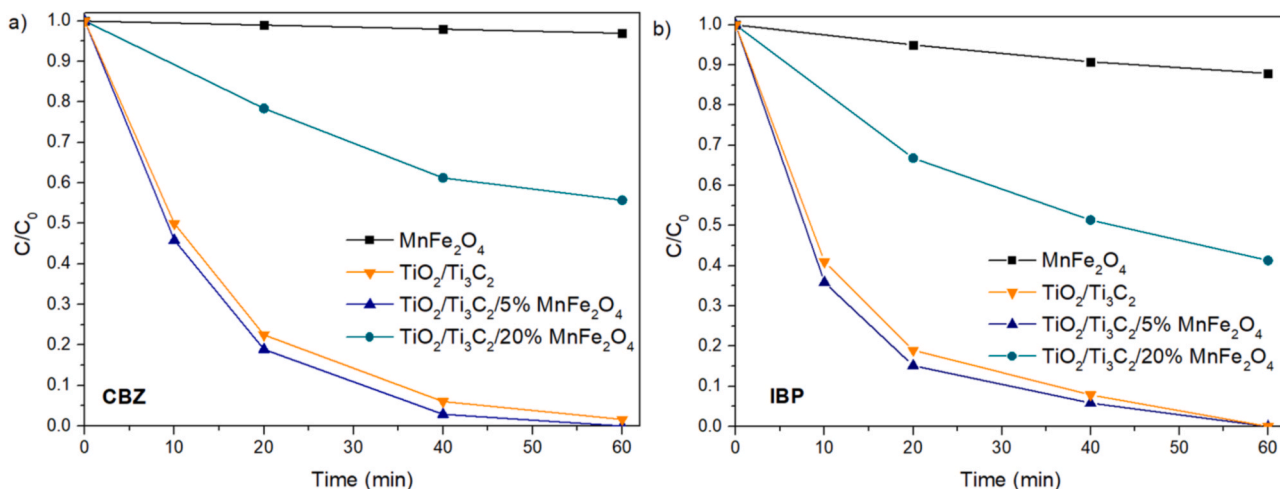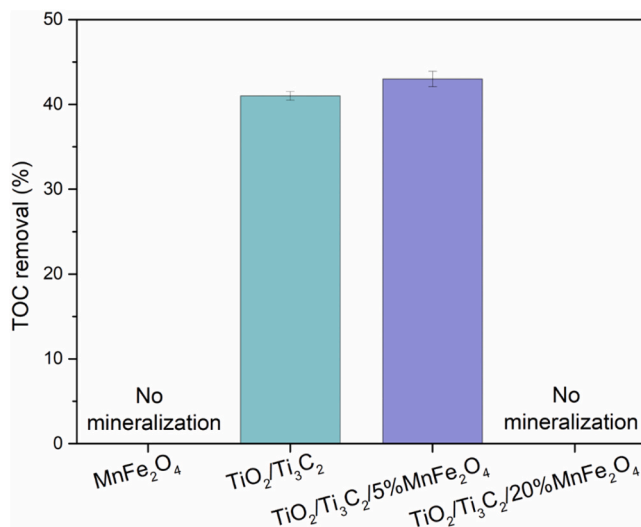**Fig. 15.** TOC removal in the photodegradation process for obtained photocatalysts.
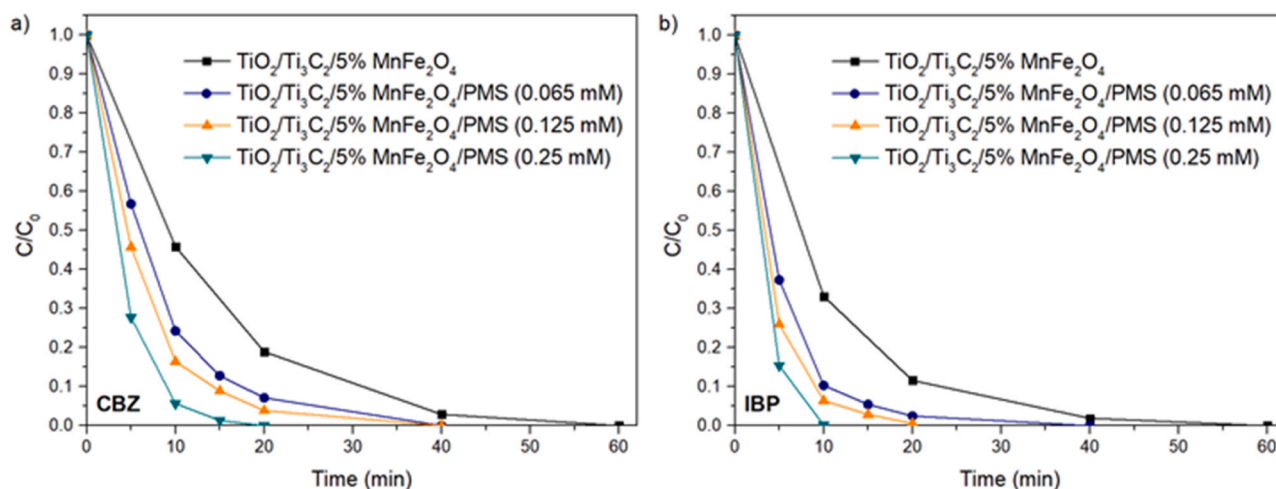

Fig. 14. The efficiency of carbamazepine (a) and ibuprofen (b) photocatalytic degradation in the CBZ/IBP mixture under simulated solar light.

Fig. 16. The effect of PMS concentration on the carbamazepine (a) and ibuprofen (b) degradation efficiency in the CBZ/IBP mixture for TiO$_2$/Ti$_3$C$_2$/5% MnFe$_2$O$_4$/PMS system.
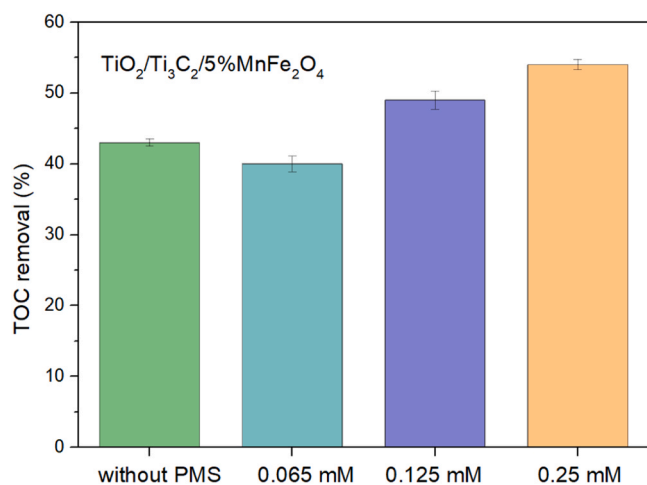

Fig. 17. The effect of PMS concentration on the carbamazepine (a) and ibuprofen (b) mineralisation efficiency measured as TOC removal for TiO$_2$/Ti$_3$C$_2$/5% MnFe$_2$O$_4$/PMS system after 60 min of irradiation.

58].

Furthermore, additional experiments were performed in the model seawater to evaluate the effect of interfering ions (Mg^{2+}, Ca^{2+}, Na$^+$ cations and Cl$^-$ and SO$_4^{2-}$) on the efficiency of CBZ and IBU photo-degradation (Fig. 20).

Interestingly, for CBZ removal, significant improvement was observed. After 5 min of irradiation, about 100% of CBZ was degraded, whereas in DI water within 20 min. The TOC removal efficiency is also summarised in Table S3 in the Supporting Materials. Also, a slight improvement in the mineralisation efficiency was observed in the model seawater. Huang et al. [59] reported that chloride ions could facilitate the Acid Orange 7 photocatalytic degradation in the presence of PMS. The enhancement could be related to the generation of reactive chlorine species from the reaction between Cl$^-$ and •SO$_4^-$ [60].

Meanwhile, for IBP, the degradation was slightly limited. The slower photodegradation of IBU in seawater compared with the DI water may be attributed to the presence of inorganic species in seawater acting as hydroxyl radical scavengers and therefore reducing photocatalytic activity [61].

In order to explain the mechanism of CBZ and IBP photodegradation with TiO$_2$/Ti$_3$C$_2$/5%MnFe$_2$O$_4$/PMS system, the trapping experiments with reactive species scavengers were performed. The results are shown in Fig. 21. The highest inhibition of CBZ degradation efficiency was
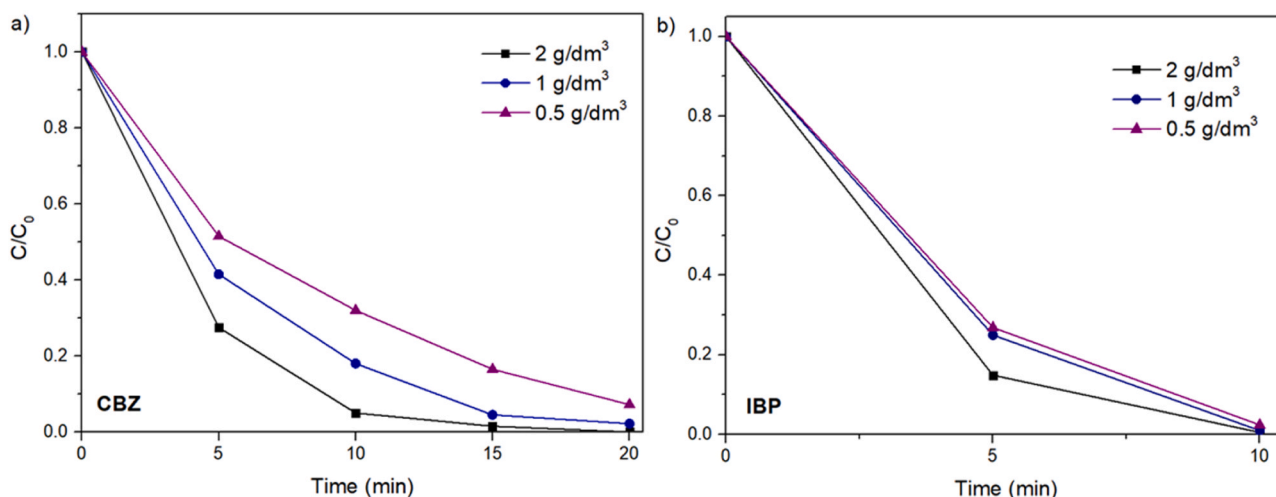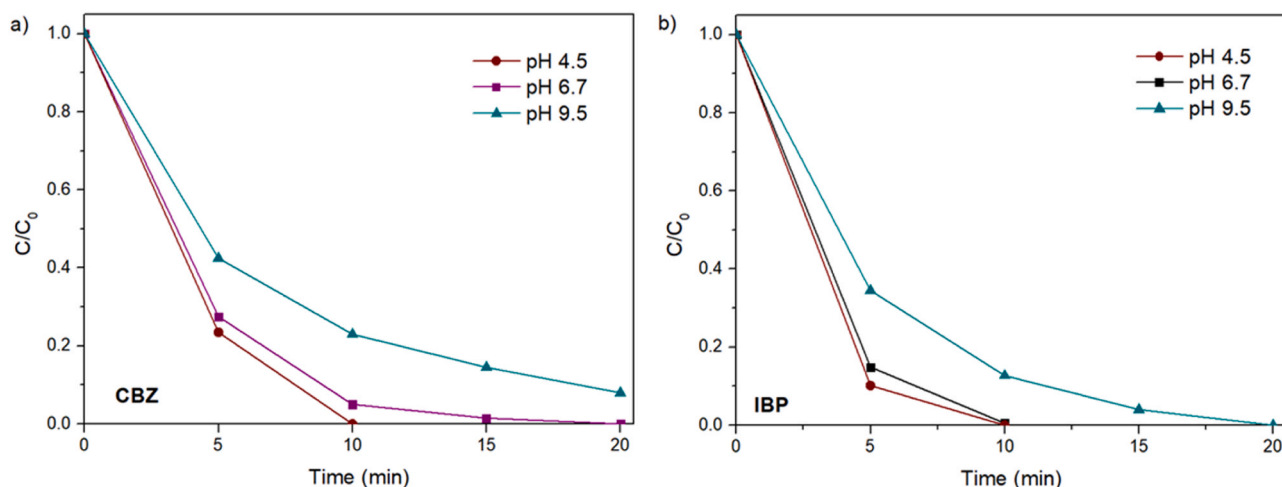

Fig. 18. The effect of photocatalyst amount on the efficiency of carbamazepine (a) and ibuprofen (b) degradation in the CBZ/IBP mixture for TiO$_2$/Ti$_3$C$_2$/5% MnFe$_2$O$_4$/PMS system.

Fig. 19. The effect of pH on the efficiency of carbamazepine (a) and ibuprofen (b) degradation (C/C_0) in the CBZ/IBP mixture for $TiO_2/Ti_3C_2/5\%$ $MnFe_2O_4/$PMS system.
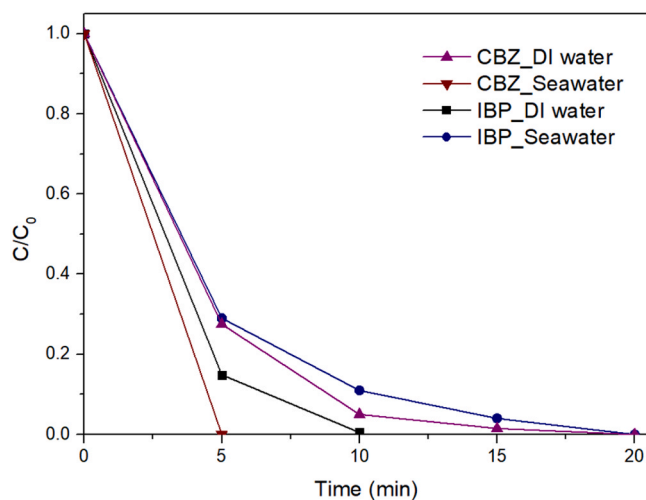

Fig. 20. The efficiency of carbamazepine and ibuprofen degradation (C/C_0) in the CBZ/IBP mixture for $TiO_2/Ti_3C_2/5\%$ $MnFe_2O_4/$PMS system in deionised water (DI) water and model seawater.

observed with the addition of benzoquinone, which indicates that superoxide anion radicals are the main oxidising species taking part in the removal of pharmaceuticals. Meanwhile, the degradation of IBP was significantly limited in the presence of ammonium oxalate. In this case, the h^+ were mainly involved in the photodegradation process. Furthermore, for both pharmaceuticals, a decrease in photocatalytic activity was observed with the addition of isopropanol, suggesting that the presence of $\bullet SO_4^-$ significantly affects the pharmaceuticals removal efficiency.

Different reactive species may play the dominant role in the photodegradation mechanism depending on the nature and physicochemical properties of both pharmaceuticals and photocatalyst. According to Dudziak et al. [62], for carbamazepine with a low energy position of LUMO orbital, the process efficiency is not exactly dependent on the stability of h^+ generated organic radical, which is frequently indicated as an initial reactive form. Meanwhile, direct h^+ transfer from the surface to the pollutant appears essential for IBU degradation, which also agrees with its preferred surface adsorption and negative charge. In the study of Georgaki et al. [63], the hole-dominated surface reaction was also observed for IBP, while for CBZ solution-phase mechanism.

The possible mechanism of pharmaceuticals degradation with $TiO_2/$$Ti_3C_2/5\%$ $MnFe_2O_4/$PMS is presented in Fig. 22. In the presence of light, the promotion of electrons from the valence band (VB) of $MnFe_2O_4$ and TiO_2 to its CB was attained in the nanocomposite, leaving behind the same number of holes in the corresponding VB. The photogenerated
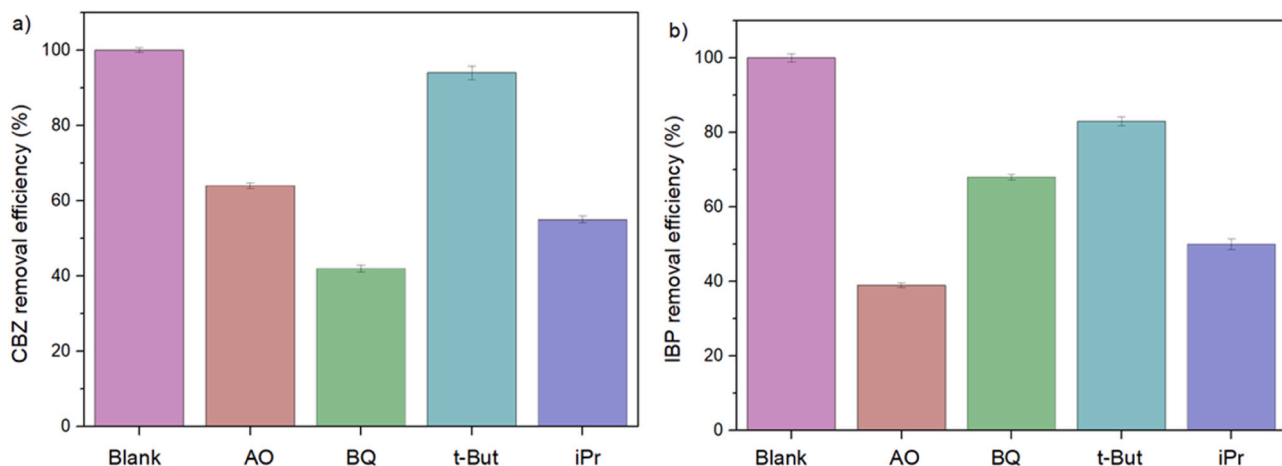

Fig. 21. The trapping experiments for carbamazepine (a) and ibuprofen (b) degradation in the CBZ/IBP mixture for $TiO_2/Ti_3C_2/5\%$ $MnFe_2O_4/$PMS system.
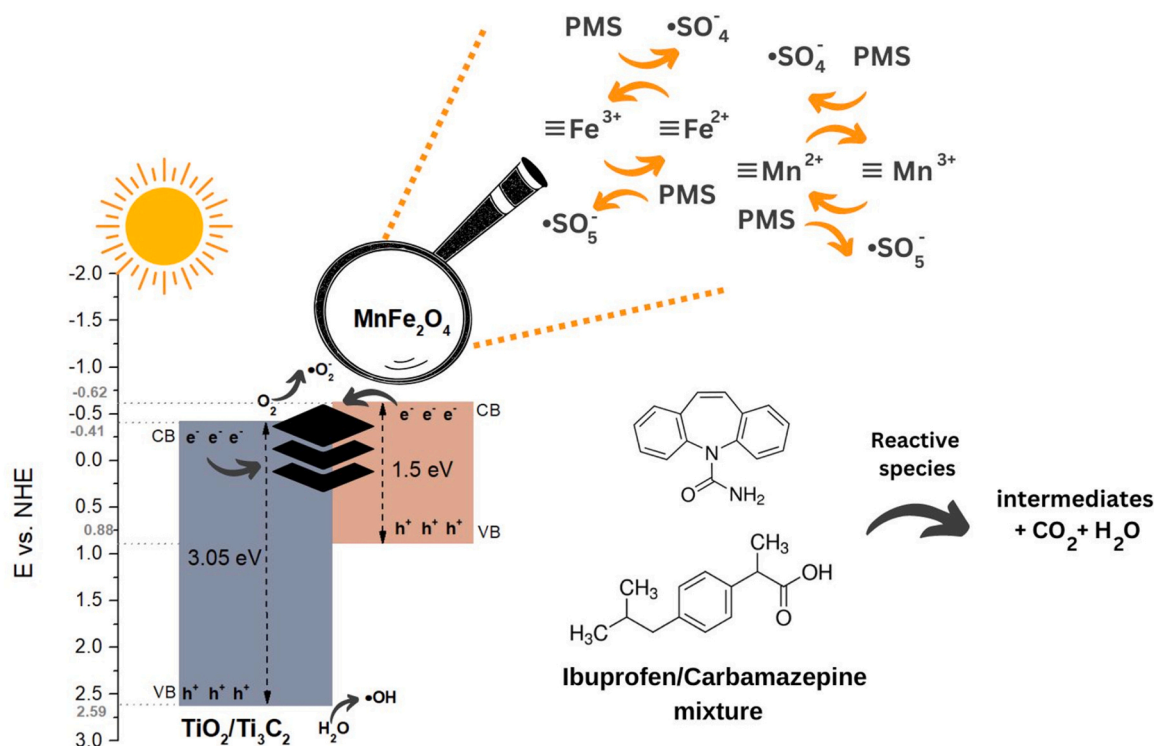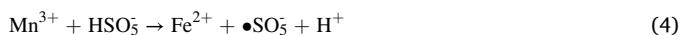
Fig. 22. The possible mechanism of IBP/CBZ mixture degradation in the presence of $TiO_2/Ti_3C_2/5\%MnFe_2O_4/PMS$.

electrons are transported to the conductive MXene at the interface, which elongates the lifetime of holes in the VB of TiO_2 and inhibits the recombination of photogenerated charge carriers. Accumulated electrons participate in superoxide anion radical generation from oxygen, whereas photogenerated holes participate in hydroxyl radicals production as a main reactive oxygen species taking part in the photocatalytic degradation of CBZ and IBP.

Furthermore, the presence of Mn and Fe may activate PMS to produce sulphate radicals. Electron transfer from PMS to Fe^{3+} and Fe^{2+} caused the regeneration of Fe^{3+} and cycling between Fe^{3+} and Fe^{2+} (Eqs. 1–2). Similarly, there was also the regeneration of Mn^{2+} and cycling between Mn^{2+} and Mn^{3+} (Eqs. 3–4). This redox cycles $Mn^{2+} \rightarrow Mn^{3+} \rightarrow Mn^{2+}$ and $Fe^{2+} \rightarrow Fe^{3+} \rightarrow Fe^{2+}$ are the rate-limiting steps in the PMS activation [64]. Furthermore, $\bullet SO_5^-$ radicals may react with each other to form $\bullet SO_4^-$ (Eq. 5). While, $\bullet SO_4^-$ may further react with OH^- to generate $\bullet OH$ (Eq. 6) [65].

$$Fe^{3+} + HSO_5^- \rightarrow Fe^{2+} + \bullet SO_5^- + H^+ \tag{1}$$

$$Fe^{2+} + HSO_5^- \rightarrow Fe^{3+} + \bullet SO_4^- + OH^- \tag{2}$$

$$Mn^{2+} + HSO_5^- \rightarrow Mn^{3+} + \bullet SO_4^- + OH^- \tag{3}$$

$$Mn^{3+} + HSO_5^- \rightarrow Fe^{2+} + \bullet SO_5^- + H^+ \tag{4}$$

$$\bullet SO_5^- + \bullet SO_5^- \rightarrow 2 \bullet SO_4^- + O_2 \tag{5}$$

$$\bullet SO_4^- + OH^- \rightarrow SO_4^{2-} + \bullet OH \tag{6}$$

Based on the ICP-OES analysis and iron photometric measurement, the levels of metal lixiviation were determined for the $TiO_2/Ti_3C_2/5\%$ $MnFe_2O_4/PMS$ system with the highest PMS concentration. The results are presented in Table S4 in the Supporting Materials. The metal lixiviation using $TiO_2/Ti_3C_2/5\%$ $MnFe_2O_4/PMS$ (0.25 mM) system to the post-process solution was below LOD for Ti, not exceeding the permissible limit for Fe (0.08 mg·dm^{-3}) in surface and drinking water, while exceeded for Mn (0.4 mg·dm^{-3}) in drinking water. Despite that, the photocatalyst showed good stability and reusability in the four subsequent cycles of photodegradation. After each cycle, the composite

material was separated and reused with no additional treatment. As presented in Fig. 23a, the degradation efficiency of CBZ and IBP remained stable and maintained at 100% within 10 min for IBP and 100% within 20 min for CBZ, respectively, confirming good stability and recyclability. Besides, the XRD characteristic peaks of the used composite are unchanged compared to the fresh material (Fig. 24a). Similarly, FTIR spectra (Fig. 24b) for $TiO_2/Ti_3C_2/5\%$ $MnFe_2O_4$ fresh sample and after the 4th photocatalytic cycle do not differ. A broad band observed in the range between 3650 and 3000 cm^{-1} with a maximum at 3430 cm^{-1} is ascribed to the stretching mode of the hydroxyl group. The characteristic signal at 1630 cm^{-1} is related to the bending vibrations of the hydroxyl group. The broad band between 882 and 400 cm^{-1} corresponds to the Ti-O stretching vibrations and Ti-O-Ti bridging stretching mode.

The results presented in the present study were compared with recent publications concerning photocatalytic degradation of IBP and CBZ enhanced by PMS activation. The comparison is presented in Table 3. However, any studies considering photocatalyst/PMS/sunlight irradiation system for IBP degradation have not been found.

4. Conclusions

For the first time, the ternary magnetic composites $TiO_2/Ti_3C_2/$ $MnFe_2O_4$ were successfully fabricated and applied for the degradation of pharmaceuticals, the mixture of carbamazepine and ibuprofen. The present work provided a new approach to the application of MXene compound as a precursor for photocatalyst synthesis and co-catalyst. The $TiO_2/Ti_3C_2/MnFe_2O_4$ magnetic composite was easily recovered from the post-process suspension after the photodegradation process by an external magnetic field. The magnetic composite revealed excellent photocatalytic activity in the wide pH range and in the presence of inorganic ions. For both pharmaceuticals, nearly 100% degradation was obtained within 60 min in the photocatalytic degradation process. The synergetic effect of the combination of photodegradation process in the presence of $TiO_2/Ti_3C_2/5\%MnFe_2O_4$ composite with PMS activation under simulated solar light was noticed. The coupling of photocatalysis
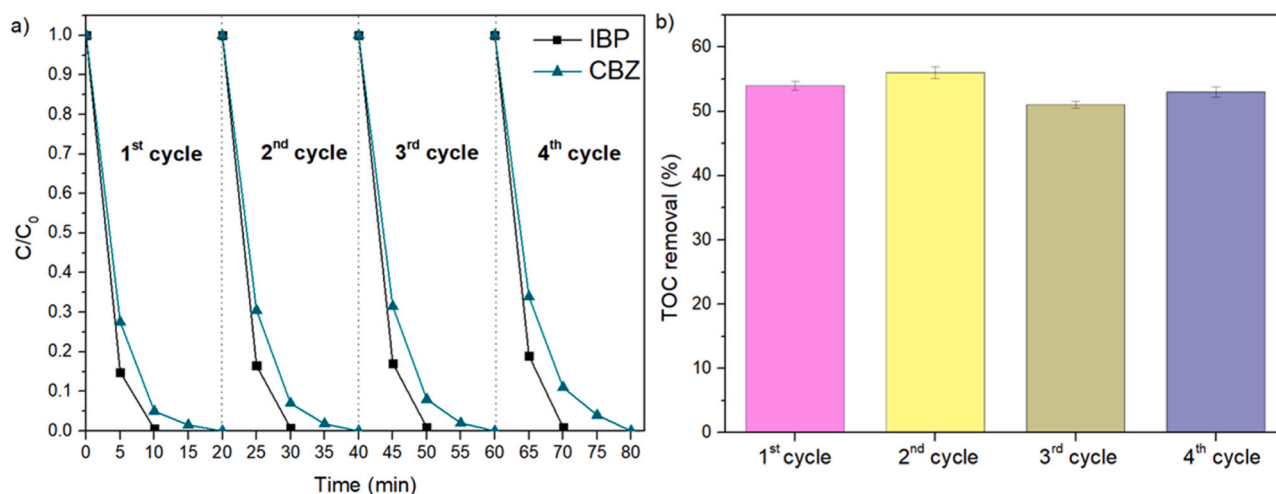
Fig. 23. The stability and reusability analyses in the four subsequent cycles of CBZ/IBP mixture photodegradation (a) and mineralisation efficiency measure as TOC reduction in the four subsequent cycles after 60 min of irradiation (b) for TiO$_2$/Ti$_3$C$_2$/5% MnFe$_2$O$_4$/PMS.
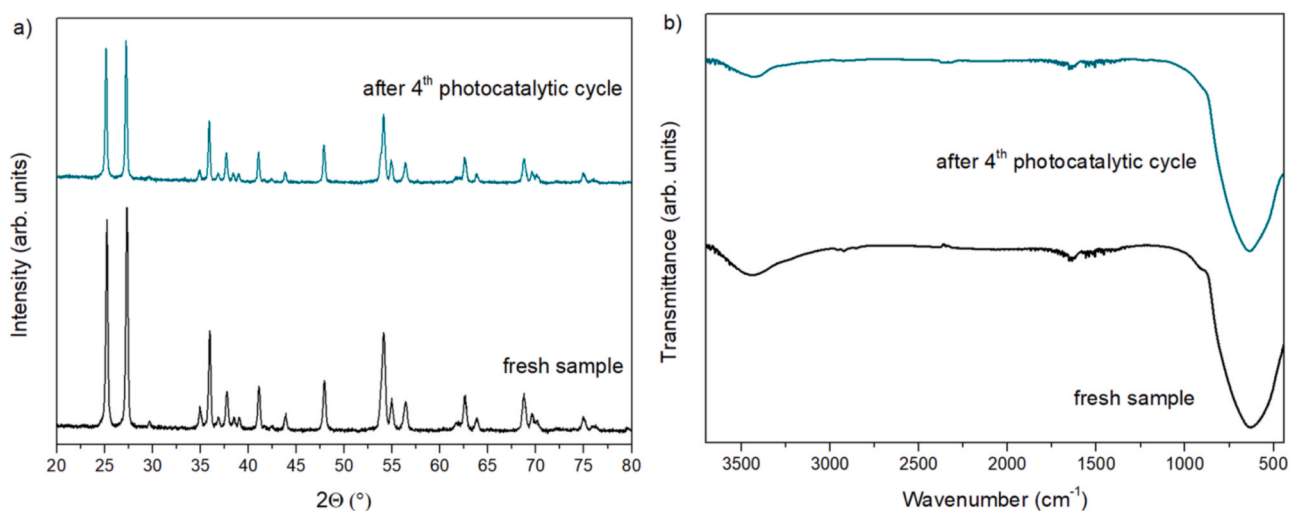
Fig. 24. The comparison of XRD diffractograms (a) and FTIR spectra (b) for TiO$_2$/Ti$_3$C$_2$/5% MnFe$_2$O$_4$ fresh sample and sample after the fourth photo-degradation cycle.

Table 3
The comparison of this work with results presented in recent related papers.

Photocatalyst	Dosage (g/dm^3)	Pharmaceutical concentration (mg/dm^3)	PMS concentration	Light source	Degradation efficiency	Ref.
BiOCl	0.6	10 (CBZ)	1 mM	simulated solar light ($\lambda > 300$ nm)	100% within 20 min	[66]
β-FeOOH on g-C$_3$N$_4$	0.1	10 (CBZ)	0.2 mM	simulated sunlight	100% within 30 min	[67]
Si-doped TiO$_2$	0.1	10 (CBZ)	1 mM	A metal halide lamp with a 300 nm cut-off filter	100% within 60 min	[68]
TiO$_2$/Ti$_3$C$_2$/5% MnFe$_2$O$_4$	2	7 (CBZ) 10 (IBP)	0.25 mM	Xe lamp	100% within 20 min 100% within 10 min	this work

with relatively low PMS concentration led to a significant increase in the kinetic of the reaction. The degradation efficiency was 100% within 20 min for carbamazepine and 10 min for ibuprofen without significant change in the pH of the solution. Therefore, considering the economic aspects related to energy saving by reducing the photocatalytic process time, combining the photocatalytic degradation process with PMS activation seems beneficial. Therefore, the results presented in this work have the potential to provide new insights into the development of combined magnetic photocatalyst/PMS processes. However, it is

important to find the compromise between high degradation efficiency in AOP-based processes and the possibility of secondary pollutants generation, for example, acidification of the treated wastewater or metal ions lixiviation into the water environment. In our study, due to the relatively low PMS concentration, we did not observe a significant change in the pH of the solution after the photodegradation process. However, for the highest PMS concentration of 0.25 mM, lixiviation of a trace amount of Fe and Mn can be noticed.

CRediT authorship contribution statement

Anna Zielińska-Jurek: Conceptualization, Methodology, Supervision, Writing – review & editing, Project administration, Funding acquisition. **Anna Grzegórska:** Formal analysis, Investigation, Visualization, Writing – review & editing. **Joseph Chibueze Ofoegbu:** Formal analysis. Diana Sannino: Writing – review & editing. **Laura Cervera-Gabalda:** Formal analysis. **Cristina Gómez-Polo:** Writing – review & editing..

Declaration of Competing Interest

The authors declare that they have no known competing financial interests or personal relationships that could have appeared to influence the work reported in this paper.

Data Availability

Data will be made available on request.

Acknowledgements

Appendix A. Supporting information

Supplementary data associated with this article can be found in the online version at doi:10.1016/j.jece.2023.110660.

References

[1] D. Camacho-Muñoz, B. Petrie, L. Lopardo, K. Proctor, J. Rice, J. Youdan, R. Barden, B. Kasprzyk-Hordern, Stereoisomeric profiling of chiral pharmaceutically active compounds in wastewaters and the receiving environment – a catchment-scale and a laboratory study, Environ. Int 127 (2019) 558–572, https://doi.org/10.1016/j.envint.2019.03.050.

[2] S. Afsa, K. Hamden, P.A. Lara Martin, H. ben Mansour, Occurrence of 40 pharmaceutically active compounds in hospital and urban wastewaters and their contribution to Mahdia coastal seawater contamination, Environ. Sci. Pollut. Res. 27 (2020) 1941–1955, https://doi.org/10.1007/s11356-019-06866-5.

[3] M. Kumar, D.D. Snow, R. Honda, S. Mukherjee, Springer Transactions in Civil and Environmental Engineering Contaminants in Drinking and Wastewater Sources Challenges and Reigning Technologies, n.d. ⟨http://www.springer.com/series/13593⟩.

[4] N.S.P. Batucan, L.A. Tremblay, G.L. Northcott, C.D. Matthaei, Medicating the environment? A critical review on the risks of carbamazepine, diclofenac and ibuprofen to aquatic organisms, Environ. Adv. 7 (2022), 100164, https://doi.org/10.1016/j.envadv.2021.100164.

[5] S. Zhu, B. Dong, Y. Wu, L. Bu, S. Zhou, Degradation of carbamazepine by vacuum-UV oxidation process: kinetics modeling and energy efficiency, J. Hazard Mater. 368 (2019) 178–185, https://doi.org/10.1016/j.jhazmat.2019.01.043.

[6] P. Paíga, M. Correia, M.J. Fernandes, A. Silva, M. Carvalho, J. Vieira, S. Jorge, J. G. Silva, C. Freire, C. Delerue-Matos, Assessment of 83 pharmaceuticals in WWTP influent and effluent samples by UHPLC-MS/MS: hourly variation, Sci. Total Environ. 648 (2019) 582–600, https://doi.org/10.1016/j.scitotenv.2018.08.129.

[7] H. Khazri, S. ben Hassine, I. Ghorbel–Abid, R. Kalfat, M. Trabelsi-Ayadi, Presence of carbamazepine, naproxen, and ibuprofen in wastewater from northern Tunisia, Environ. Forensics 20 (2019) 121–128, https://doi.org/10.1080/15275922.2019.1597779.

[8] B. Björlenius, M. Ripszám, P. Haglund, R.H. Lindberg, M. Tysklind, J. Fick, Pharmaceutical residues are widespread in Baltic Sea coastal and offshore waters – screening for pharmaceuticals and modelling of environmental concentrations of carbamazepine, Sci. Total Environ. 633 (2018) 1496–1509, https://doi.org/10.1016/j.scitotenv.2018.03.276.

[9] A. González-Mira, A. Torreblanca, F. Hontoria, J.C. Navarro, E. Mañanós, I. Varó, Effects of ibuprofen and carbamazepine on the ion transport system and fatty acid metabolism of temperature conditioned juveniles of Solea senegalensis, Ecotoxicol. Environ. Saf. 148 (2018) 693–701, https://doi.org/10.1016/j.ecoenv.2017.11.023.

[10] D. Ghime, P. Ghosh, Advanced oxidation processes: a powerful treatment option for the removal of recalcitrant organic compounds, in: Advanced Oxidation Processes - Applications, Trends, and Prospects, IntechOpen, 2020, https://doi.org/10.5772/intechopen.90192.

[11] A. Fiszka Borzyszkowska, A. Pieczyńska, A. Ofiarska, W. Lisowski, K. Nikiforow, E. M. Siedlecka, Photocatalytic degradation of 5-fluorouracil in an aqueous environment via Bi–B co-doped TiO₂ under artificial sunlight, Int. J. Environ. Sci. Technol. 17 (2020) 2163–2176, https://doi.org/10.1007/s13762-019-02604-z.

[12] H. Farzaneh, K. Loganathan, J. Saththasivam, G. McKay, Ozone and ozone/hydrogen peroxide treatment to remove gemfibrozil and ibuprofen from treated sewage effluent: factors influencing bromate formation, Emerg. Contam. 6 (2020) 225–234, https://doi.org/10.1016/j.emcon.2020.06.002.

[13] J.-K. Im, I.-H. Cho, S.-K. Kim, K.-D. Zoh, Optimization of carbamazepine removal in O₃/UV/H₂O₂ system using a response surface methodology with central composite design, Desalination 285 (2012) 306–314, https://doi.org/10.1016/j.desal.2011.10.018.

[14] S. Sun, H. Yao, W. Fu, F. Liu, X. Wang, W. Zhang, Enhanced degradation of carbamazepine in FeOCl based Photo-Fenton reaction, J. Environ. Chem. Eng. 9 (2021), 104501, https://doi.org/10.1016/j.jece.2020.104501.

[15] A. Fiszka Borzyszkowska, A. Sulowska, I. Zekker, J. Karczewski, K. Bester, A. Zielińska-Jurek, Environmentally friendly fabrication of high-efficient Fe-ZnO/citric acid-modified cellulose composite and the enhancement of photocatalytic activity in the presence of H₂O₂, Catalysts 12 (2022) 1370, https://doi.org/10.3390/catal12111370.

[16] S. Sun, H. Yao, W. Fu, F. Liu, X. Wang, W. Zhang, Enhanced degradation of carbamazepine in FeOCl based Photo-Fenton reaction, J. Environ. Chem. Eng. 9 (2021), 104501, https://doi.org/10.1016/j.jece.2020.104501.

[17] S. Venkatesh, K. Venkatesh, A.R. Quaff, Dye decomposition by combined ozonation and anaerobic treatment: cost effective technology, J. Appl. Res. Technol. 15 (2017) 340–345, https://doi.org/10.1016/j.jart.2017.02.006.

[18] J. Gomes, R. Costa, R.M. Quinta-Ferreira, R.C. Martins, Application of ozonation for pharmaceuticals and personal care products removal from water, Sci. Total Environ. 586 (2017) 265–283, https://doi.org/10.1016/j.scitotenv.2017.01.216.

[19] R. Saravanan, F. Gracia, A. Stephen, Basic principles (in:), Mech., Chall. Photocatal. (2017) 19–40, https://doi.org/10.1007/978-3-319-62446-4_2.

[20] R. Marschall, Semiconductor composites: strategies for enhancing charge carrier separation to improve photocatalytic activity, Adv. Funct. Mater. 24 (2014) 2421–2440, https://doi.org/10.1002/adfm.201303214.

[21] A. Grzegórska, P. Głuchowski, J. Karczewski, J. Ryl, I. Wysocka, K. Siuzdak, G. Trykowski, K. Grochowska, A. Zielińska-Jurek, Enhanced photocatalytic activity of accordion-like layered Ti₃C₂ (MXene) coupled with Fe-modified decahedral anatase particles exposing {1 0 1} and {0 0 1} facets, Chem. Eng. J. 426 (2021), https://doi.org/10.1016/j.cej.2021.130801.

[22] A. Grzegórska, A. Gajewicz-Skretna, G. Trykowski, K. Sikora, A. Zielińska-Jurek, Design and synthesis of TiO₂/Ti₃C₂ composites for highly efficient photocatalytic removal of acetaminophen: the relationships between synthesis parameters, physicochemical properties, and photocatalytic activity, Catal. Today (2022), https://doi.org/10.1016/j.cattod.2022.12.011.

[23] C. Peng, X. Xie, W. Xu, T. Zhou, P. Wei, J. Jia, K. Zhang, Y. Cao, H. Wang, F. Peng, R. Yang, X. Yan, H. Pan, H. Yu, Engineering highly active Ag/Nb₂O₅@Nb₂CTₓ (MXene) photocatalysts via steering charge kinetics strategy, Chem. Eng. J. 421 (2021), https://doi.org/10.1016/j.cej.2021.128766.

[24] Y. Wang, X. Hu, H. Song, Y. Cai, Z. Li, D. Zu, P. Zhang, D. Chong, N. Gao, Y. Shen, C. Li, Oxygen vacancies in actiniae-like Nb₂O₅/Nb₂C MXene heterojunction boosting visible light photocatalytic NO removal, Appl. Catal. B. 299 (2021), https://doi.org/10.1016/j.apcatb.2021.120677.

[25] A.M. Chávez, R.R. Solís, F.J. Beltrán, Magnetic graphene TiO₂-based photocatalyst for the removal of pollutants of emerging concern in water by simulated sunlight aided photocatalytic ozonation, Appl. Catal. B. 262 (2020), 118275, https://doi.org/10.1016/j.apcatb.2019.118275.

[26] Z. Lendzion-Bieluń, A. Wojciechowska, J. Grzechulska-Damszel, U. Narkiewicz, Z. Śniadecki, B. Idzikowski, Effective processes of phenol degradation on Fe₃O₄–TiO₂ nanostructured magnetic photocatalyst, J. Phys. Chem. Solids 136 (2020), 109178, https://doi.org/10.1016/j.jpcs.2019.109178.

[27] K.K. Kefeni, B.B. Mamba, Photocatalytic application of spinel ferrite nanoparticles and nanocomposites in wastewater treatment: Review, Sustain. Mater. Technol. 23 (2020), e00140, https://doi.org/10.1016/j.susmat.2019.e00140.

[28] R. Suresh, S. Rajendran, P.S. Kumar, D.-V. Vo, L. Cornejo-Ponce, Recent advancements of spinel ferrite based binary nanocomposite photocatalysts in wastewater treatment, Chemosphere 274 (2021), 129734, https://doi.org/10.1016/j.chemosphere.2021.129734.

[29] B. Mandal, J. Panda, P.K. Paul, R. Sarkar, B. Tudu, MnFe₂O₄ decorated reduced graphene oxide heterostructures: nanophotocatalyst for methylene blue dye degradation, Vacuum 173 (2020), https://doi.org/10.1016/j.vacuum.2019.109150.

[30] W. Han, D. Li, M. Zhang, H. Ximin, X. Duan, S. Liu, S. Wang, Photocatalytic activation of peroxymonosulfate by surface-tailored carbon quantum dots, J. Hazard Mater. 395 (2020), https://doi.org/10.1016/j.jhazmat.2020.122695.

[31] W. Shi, Y. Liu, W. Sun, Y. Hong, X. Li, X. Lin, F. Guo, J. Shi, Assembling g-C₃N₄ nanosheets on rod-like CoFe₂O₄ nanocrystals to boost photocatalytic degradation of ciprofloxacin with peroxymonosulfate activation, Mater. Today Commun. 29 (2021), https://doi.org/10.1016/j.mtcomm.2021.102871.

[32] J. Li, X. Cheng, H. Zhang, J. Gou, X. Zhang, D. Wu, D.D. Dionysiou, Insights into performance and mechanism of ZnO/CuCo₂O₄ composite as heterogeneous photoactivator of peroxymonosulfate for enrofloxacin degradation, J. Hazard Mater. 448 (2023), 130946, https://doi.org/10.1016/j.jhazmat.2023.130946.

[33] M.G. Antoniou, A.A. de la Cruz, D.D. Dionysiou, Degradation of microcystin-LR using sulfate radicals generated through photolysis, thermolysis and e⁻ transfer mechanisms, Appl. Catal. B. 96 (2010) 290–298, https://doi.org/10.1016/j.apcatb.2010.02.013.

[34] V. Hasija, P. Raizada, V.K. Thakur, T. Ahamad, S.M. Alshehri, S. Thakur, V. H. Nguyen, Q. van Le, P. Singh, An overview on photocatalytic sulfate radical formation via doped graphitic carbon nitride for water remediation, Curr. Opin. Chem. Eng. 37 (2022), 100841, https://doi.org/10.1016/j.coche.2022.100841.

[35] X. Tan, J. Bai, J. Zheng, Y. Zhang, J. Li, T. Zhou, L. Xia, Q. Xu, B. Zhou, Photocatalytic fuel cell based on sulfate radicals converted from sulfates in situ for wastewater treatment and chemical energy utilisation, Catal. Today 335 (2019) 485–491, https://doi.org/10.1016/j.cattod.2019.02.014.

[36] B. Cao, S. Wan, Y. Wang, H. Guo, M. Ou, Q. Zhong, Highly-efficient visible-light-driven photocatalytic H_2 evolution integrated with microplastic degradation over MXene/$Zn_xCd_{1-x}S$ photocatalyst, J. Colloid Interface Sci. 605 (2022) 311–319, https://doi.org/10.1016/j.jcis.2021.07.113.

[37] S. Cao, B. Shen, T. Tong, J. Fu, J. Yu, 2D/2D heterojunction of ultrathin MXene/ Bi_2WO_6 nanosheets for improved photocatalytic CO_2 reduction, Adv. Funct. Mater. 28 (2018), 1800136, https://doi.org/10.1002/adfm.201800136.

[38] Y. Cao, Q. Deng, Z. Liu, D. Shen, T. Wang, Q. Huang, S. Du, N. Jiang, C.-T. Lin, J. Yu, Enhanced thermal properties of poly(vinylidene fluoride) composites with ultrathin nanosheets of MXene, RSC Adv. 7 (2017) 20494–20501, https://doi.org/10.1039/C7RA04184C.

[39] W.Y. Chen, X. Jiang, S.-N. Lai, D. Peroulis, L. Stanciu, Nanohybrids of a MXene and transition metal dichalcogenide for selective detection of volatile organic compounds, Nat. Commun. 11 (2020) 1302, https://doi.org/10.1038/s41467-020-15092-4.

[40] D. Xu, Z. Li, L. Li, J. Wang, Insights into the photothermal conversion of 2D MXene nanomaterials: synthesis, mechanism, and applications, Adv. Funct. Mater. 30 (2020), 2000712, https://doi.org/10.1002/adfm.202000712.

[41] P. Kommu, R. Dash, G.P. Singh, A.S. Bhattacharyya, Mixed transitional metal oxide of $MnFe_2O_4$ synthesised by solution combustion method and their electrochemical applications, Energy Storage (2022), https://doi.org/10.1002/est2.423.

[42] F. Jelokhani, S. Sheibani, A. Ataie, Adsorption and photocatalytic characteristics of cobalt ferrite-reduced graphene oxide and cobalt ferrite-carbon nanotube nanocomposites, J. Photochem. Photobio. A Chem. 403 (2020), 112867, https://doi.org/10.1016/j.jphotochem.2020.112867.

[43] H. Qin, Y. Yang, W. Shi, Y. She, Heterogeneous Fenton degradation of ofloxacin catalysed by magnetic nanostructured $MnFe_2O_4$ with different morphologies, Environ. Sci. Pollut. Res. 28 (2021) 26558–26570, https://doi.org/10.1007/s11356-021-12548-y.

[44] A. Iqbal, U. Saidu, S. Sreekantan, M.N. Ahmad, M. Rashid, N.M. Ahmed, W. H. Danial, L.D. Wilson, Mesoporous TiO_2 implanted ZnO QDs for the photodegradation of tetracycline: material design, structural characterisation and photodegradation mechanism, Catalysts 11 (2021) 1205, https://doi.org/10.3390/catal11101205.

[45] Y. Sun, Y. Sun, X. Meng, Y. Gao, Y. Dall'Agnese, G. Chen, C. Dall'Agnese, X.-F. Wang, Eosin Y-sensitized partially oxidised Ti_3C_2 MXene for photocatalytic hydrogen evolution, Catal. Sci. Technol. 9 (2019) 310–315, https://doi.org/10.1039/C8CY02240B.

[46] T.M. Hammad, J.K. Salem, A.A. Amsha, N.K. Hejazy, Optical and magnetic characterisations of zinc substituted copper ferrite synthesised by a co-precipitation chemical method, J. Alloy. Compd. 741 (2018) 123–130, https://doi.org/10.1016/j.jallcom.2018.01.123.

[47] N. Pradhan, Red-tuned Mn d-d emission in doped semiconductor nanocrystals, ChemPhysChem 17 (2016) 1087–1094, https://doi.org/10.1002/cphc.201500953.

[48] B. Boutra, N. Güy, M. Özacar, M. Trari, Magnetically separable $MnFe_2O_4$/TA/ZnO nanocomposites for photocatalytic degradation of Congo Red under visible light, J. Magn. Magn. Mater. 497 (2020), 165994, https://doi.org/10.1016/j.jmmm.2019.165994.

[49] J. Qu, J. He, H. Li, Q. Jiang, M. Li, Q. Kong, M. Shi, R. Li, C. Li, Unraveling the role of interface in photogenerated charge separation at the anatase/rutile heterophase junction, J. Phys. Chem. C. 127 (2023) 768–775, https://doi.org/10.1021/acs.jpcc.2c07482.

[50] W.K. Wang, J.J. Chen, X. Zhang, Y.X. Huang, W.W. Li, H.Q. Yu, Self-induced synthesis of phase-junction TiO_2 with a tailored rutile to anatase ratio below phase transition temperature, Sci. Rep. 6 (2016) 20491, https://doi.org/10.1038/srep20491.

[51] R. Quesada-Cabrera, C. Sotelo-Vazquez, J.C. Bear, J.A. Darr, I.P. Parkin, Photocatalytic evidence of the rutile-to-anatase electron transfer in titania, Adv. Mater. Interfaces 1 (2014), 1400069, https://doi.org/10.1002/admi.201400069.

[52] Y. Chen, Z. Jiang, L. Xu, C. Liu, Y. Cheng, Y. Zou, Q. Zhang, Composite magnetic photocatalyst $Bi_{24}O_{31}Br_{10}$/$NiFe_2O_4$: Hydrothermal preparation, characterisation and photocatalytic mechanism, Mater. Sci. Semicond. Process 126 (2021), https://doi.org/10.1016/j.mssp.2021.105669.

[53] M. Li, C. Song, Y. Wu, M. Wang, Z. Pan, Y. Sun, L. Meng, S. Han, L. Xu, L. Gan, Novel Z-scheme visible-light photocatalyst based on $CoFe_2O_4$/BiOBr/Graphene composites for organic dye degradation and Cr(VI) reduction, Appl. Surf. Sci. 478 (2019) 744–753, https://doi.org/10.1016/j.apsusc.2019.02.017.

[54] H.L. So, K.Y. Lin, W. Chu, H. Gong, Degradation of triclosan by recyclable $MnFe_2O_4$-activated PMS: process modification for reduced toxicity and enhanced performance, Ind. Eng. Chem. Res 59 (2020) 4257–4264, https://doi.org/10.1021/acs.iecr.9b05481.

[55] G. Chen, X. Zhang, Y. Gao, G. Zhu, Q. Cheng, X. Cheng, Novel magnetic MnO_2/ $MnFe_2O_4$ nanocomposite as a heterogeneous catalyst for activation of peroxymonosulfate (PMS) toward oxidation of organic pollutants, Sep Purif. Technol. 213 (2019) 456–464, https://doi.org/10.1016/j.seppur.2018.12.049.

[56] L. Zhu, Z. Shi, L. Deng, Y. Duan, Efficient degradation of sulfadiazine using magnetically recoverable $MnFe_2O_4$/δ-MnO_2 hybrid as a heterogeneous catalyst of peroxymonosulfate, Colloids Surf. A Physicochem Eng. Asp. 609 (2021), 125637, https://doi.org/10.1016/j.colsurfa.2020.125637.

[57] M. Ahmadi, F. Ghanbari, M. Moradi, Photocatalysis assisted by peroxymonosulfate and persulfate for benzotriazole degradation: effect of pH on sulfate and hydroxyl radicals, Water Sci. Technol. 72 (2015) 2095–2102, https://doi.org/10.2166/wst.2015.437.

[58] X. Liu, J. Zhou, D. Liu, L. Li, W. Liu, S. Liu, C. Feng, Construction of Z-scheme $CuFe_2O_4$/MnO_2 photocatalyst and activating peroxymonosulfate for phenol degradation: synergistic effect, degradation pathways, and mechanism, Environ. Res 200 (2021), 111736, https://doi.org/10.1016/j.envres.2021.111736.

[59] Y. Huang, Q. Jiang, X. Yu, H. Gan, X. Zhu, Y. Su, Z. Xu, C. He, A combined radical and non-radical oxidation processes for efficient degradation of Acid Orange 7 in the homogeneous Cu(II)/PMS system: important role of chloride, Environ. Sci. Pollut. Res. 28 (2021) 51251–51264, https://doi.org/10.1007/s11356-021-14262-1.

[60] H. Ming, D. Wei, Y. Yang, B. Chen, C. Yang, J. Zhang, Y. Hou, Photocatalytic activation of peroxymonosulfate by carbon quantum dots functionalised carbon nitride for efficient degradation of bisphenol A under visible-light irradiation, Chem. Eng. J. 424 (2021), 130296, https://doi.org/10.1016/j.cej.2021.130296.

[61] C.C. Yang, C.L. Huang, T.C. Cheng, H.T. Lai, Inhibitory effect of salinity on the photocatalytic degradation of three sulfonamide antibiotics, Int Biodeterior. Biodegrad. 102 (2015) 116–125, https://doi.org/10.1016/j.ibiod.2015.01.015.

[62] S. Dudziak, A. Fiszka Borzyszkowska, A. Zielińska-Jurek, Photocatalytic degradation and pollutant-oriented structure-activity analysis of carbamazepine, ibuprofen and acetaminophen over faceted TiO_2, J. Environ. Chem. Eng. 11 (2023), 109553, https://doi.org/10.1016/j.jece.2023.109553.

[63] I. Georgaki, E. Vasilaki, N. Katsarakis, A study on the degradation of carbamazepine and ibuprofen by TiO_2 & ZnO Photocatalysis upon UV/visible-light irradiation, Am. J. Anal. Chem. 05 (2014) 518–534, https://doi.org/10.4236/ajac.2014.58060.

[64] Z. Xie, D.D. Dionysiou, S. Luo, M. Chen, Z. Wei, Dual-reaction center catalyst based on common metals Cu-Mg-Al for synergistic peroxymonosulfate adsorption-activation in Fenton-like process, Appl. Catal. B. 327 (2023), 122468, https://doi.org/10.1016/j.apcatb.2023.122468.

[65] M. Long, D. Li, H. Li, X. Ma, Q. Zhao, Q. Wen, F. Song, Synergetic effect of photocatalysis and peroxymonosulfate activated by MFe_2O_4 (M = Co, Mn, or Zn) for enhanced photocatalytic activity under visible light irradiation, RSC Adv. 12 (2022) 20946–20955, https://doi.org/10.1039/D2RA03558H.

[66] Y. Fang, H. Wang, X. Wang, Y. Zhou, L. Wu, W. Duo Wu, Z. Wu, Constructing thin BiOCl nanoplates for highly efficient photocatalytic peroxymonosulfate activation: in-depth understanding of the activation process, Sep Purif. Technol. 307 (2023), 122771, https://doi.org/10.1016/j.seppur.2022.122771.

[67] X. Wang, W. Lu, Z. Zhao, H. Zhong, Z. Zhu, W. Chen, In situ stable growth of β-FeOOH on g-C_3N_4 for deep oxidation of emerging contaminants by photocatalytic activation of peroxymonosulfate under solar irradiation, Chem. Eng. J. 400 (2020), 125867, https://doi.org/10.1016/j.cej.2020.125872.

[68] Y. Zhou, H. Zhang, L. Wu, Y. Zhang, X. Wang, Z. Wu, Hollow hemispherical Si-doped anatase for efficient carbamazepine degradation via photocatalytic activation of peroxymonosulfate, Chem. Eng. J. 457 (2023), 141234, https://doi.org/10.1016/j.cej.2022.141234.